

# New magnetic chemically peculiar stars and candidates in the ATLAS First Catalog of Variable Stars

Klaus Bernhard,<sup>1,2\*</sup> Stefan Hümmerich,<sup>1,2</sup> Ernst Paunzen<sup>3</sup> and Johana Supíková<sup>4</sup>

<sup>1</sup>Bundesdeutsche Arbeitsgemeinschaft für Veränderliche Sterne e.V. (BAV), Munsterdamm 90, D-12169 Berlin, Germany

<sup>2</sup>American Association of Variable Star Observers (AAVSO), 49 Bay State Rd, Cambridge, MA 02138, USA

<sup>3</sup>Department of Theoretical Physics and Astrophysics, Masaryk University, Kotlářská 2, 611 37 Brno, Czech Republic

<sup>4</sup>Faculty of Informatics, Masaryk University, Botanická 68A, 602 00 Brno, Czech Republic

arXiv:2107.07990v1 [astro-ph.SR] 16 Jul 2021

Accepted XXX. Received YYY; in original form ZZZ

## ABSTRACT

The number of known variable stars has increased by several magnitudes over the last decade, and automated classification routines are becoming increasingly important to cope with this development. Here we show that the ‘upside-down CBH variables’, which were proposed as a potentially new class of variable stars by Heinze et al. (2018) in the ATLAS First Catalogue of Variable Stars, are, at least to a high percentage, made up of  $\alpha^2$  Canum Venaticorum (ACV) variables – that is, photometrically variable magnetic chemically peculiar (CP2/He-peculiar) stars – with distinct double-wave light curves. Using suitable selection criteria, we identified 264 candidate ACV variables in the ATLAS variable star catalogue. 62 of these objects were spectroscopically confirmed with spectra from the Large Sky Area Multi-Object Fiber Spectroscopic Telescope (all new discoveries except for nine stars) and classified on the MK system. The other 202 stars are here presented as ACV star candidates that require spectroscopic confirmation. The vast majority of our sample of stars are main-sequence objects. Derived masses range from  $1.4 M_{\odot}$  to  $5 M_{\odot}$ , with half our sample stars being situated in the range from  $2 M_{\odot}$  to  $2.4 M_{\odot}$ , in good agreement with the spectral classifications. Most stars belong to the thin or thick disk; four objects, however, classify as members of the halo population. With a peak magnitude distribution at around 14th magnitude, the here presented stars are situated at the faint end of the known Galactic mCP star population. Our study highlights the need to consider rare variability classes, like ACV variables, in automated classification routines.

**Key words:** stars: chemically peculiar – stars: variables: general

## 1 INTRODUCTION

Over the last decades, rapid advances in technology and the resulting increasing number of large-scale digital sky surveys have helped to propel astronomy into a new data-rich era (Djorgovski et al. 2013). This development necessitated the invention of novel ways to deal with the amount of incoming data produced by the petabyte-scale sky surveys, and algorithmic advances in the automated handling of massive and complex data sets have become of great importance.

The field of variable star research is no exception and has greatly benefited from the increasing amount of available photometric time-series data, which are often made available in real time. The number of known variable stars has increased by several magnitudes over the last decade alone, with recent variable star catalogues containing hundreds of thousands of entries (e.g. Heinze et al. 2018; Chen et al. 2020) and the International Variable Star Index (VSX; Watson 2006) of the American Association of Variable Star Observers (AAVSO), the most coherent and up-to-date database of variable stars, cataloging more than 2,100,000 objects at the time of this writing (June 2021). Automated classification routines are of essential importance to sort the vast number of newly discovered variable stars into as-

trophysically meaningful classes. However, with the development of new and improved algorithms and classification networks, new (meta)classes are constantly developed, and it is not easy to keep track with this steadily growing body of nomenclature.

In agreement with the general trend, an increasingly large number of photometrically variable chemically peculiar (CP) stars have been identified during the past decades (e.g. Paunzen & Maitzen 1998; Wright et al. 2012; Bernhard et al. 2015a,b; Hümmerich et al. 2016; Bowman et al. 2018; Hümmerich et al. 2018; David-Uraz et al. 2019; Sikora et al. 2019). CP stars are upper main-sequence objects, which are generally found between spectral types early B to early F and characterised by peculiar surface abundances. The observed peculiarities are thought to have their origin in the interplay between radiative levitation and gravitational settling (atomic diffusion) in the calm outer layers of slowly rotating stars (e.g. Michaud 1970; Richer et al. 2000). Several types of CP stars exist, such as the metallic-line or Am/CP1 stars, the magnetic Ap/CP2 stars, the HgMn/CP3 stars, and the He-peculiar stars, which are composed of the CP4/He-weak stars and the He-rich stars (Preston 1974). Relevant to the present investigation are the CP2 and the He-pec stars, which generally exhibit strong and globally organised magnetic fields and atmospheres selectively enriched in elements such as Si, Cr, Sr, or Eu. These objects are frequently grouped together under the term of magnetic chemically

\* E-mail: klaus.bernhard@liwest.at (KB)

peculiar (mCP) stars, which, for convenience, we will adhere to in the present study.

Magnetic CP stars usually present a non-uniform surface distribution of chemical elements (chemical spots or belts). Flux is redistributed in these structures via line and continuum blanketing (e.g. Lanz et al. 1996; Shulyak et al. 2010), which results in strictly periodic light and spectral variations with the rotation period. After their bright prototype, photometrically variable mCP stars are also referred to as  $\alpha^2$  Canum Venaticorum (ACV) variables. Observed amplitudes of the photometric variability are generally of the order of several hundredths of a magnitude in the optical region, occasionally reaching up to about 0.2 mag ( $V$ ). In the ‘zoo’ of variable stars, ACV variables constitute a rather obscure class and, in automated classification systems, are often combined with other rotational variables under generic types, such as ‘ROT’ (i.e. spotted stars not classified into a particular class), or get largely ignored.

Here we show that the ‘upside-down CBH variables’<sup>1</sup>, identified through the analysis of data from the Asteroid Terrestrial-impact Last Alert System (ATLAS) and proposed by Heinze et al. (2018) in the ATLAS variable star Data Release One (ATLAS DR1) catalogue as a potentially new class of variable stars, are, at least to a high percentage, made up of ACV variables with distinct double-wave light curves. Using suitable selection criteria, we identified 264 candidate ACV variables in the ATLAS DR1 catalogue. 62 of these stars could be confirmed as mCP stars (53 new discoveries) using spectra from the Large Sky Area Multi-Object Fiber Spectroscopic Telescope (LAMOST) and were classified on the MK system.

Data sources, motivation and the process of target selection are detailed in Section 2. Spectral classifications are described and presented in Section 3. The magnitude, period and space distributions of our sample stars are investigated in Section 4, while Section 5 explores the ages and masses of our sample stars. We conclude in Section 6.

## 2 DATA SOURCES, MOTIVATION AND TARGET SELECTION

### 2.1 The Asteroid Terrestrial-impact Last Alert System (ATLAS)

The Asteroid Terrestrial-impact Last Alert System (ATLAS) is a NASA-funded sky survey developed by the University of Hawaii with the main aim of discovering potentially hazardous near-Earth asteroids (NEAs). It currently consists of two telescopes, which are situated on Haleakala and Mauna Loa and equipped with f/2.0 0.5-m DFM custom Wright Schmidt telescopes and STA-1600 10.5x10.5k CCD detectors. The telescopes command a field of view with a diameter of  $7.4'$ , and observations are procured through two broadband filters: the cyan filter (‘c’; 420–650 nm), which is employed during the two weeks surrounding the new Moon, and the orange filter (‘o’; 560–820 nm), which is used in lunar bright time. Both filters are linked via colour transformations to the Pan-STARRS  $g$ ,  $r$ , and  $i$  bands. More information on the ATLAS sky survey is found in Tonry et al. (2018).

<sup>1</sup> For convenience, in the text, these objects are hereafter referred to as ud-CBH variables.

### 2.2 The Large Sky Area Multi-Object Fiber Spectroscopic Telescope (LAMOST)

The LAMOST telescope (Zhao et al. 2012; Cui et al. 2012), also called the Guo Shou Jing<sup>2</sup> Telescope, is a reflecting Schmidt telescope located at the Xinglong Observatory in Beijing, China. It boasts an effective aperture of 3.6–4.9 m and a field of view of  $5^\circ$ . Thanks to its unique design, LAMOST is able to take 4000 spectra in a single exposure with spectral resolution  $R \sim 1800$ , limiting magnitude  $r \sim 19$  mag and wavelength coverage from 3700 Å to 9000 Å. LAMOST is therefore particularly suited to survey large portions of the sky and is dedicated to a spectral survey of the entire available northern sky. LAMOST data products are released to the public in consecutive data releases and can be accessed via the LAMOST spectral archive.<sup>3</sup> With about 10 million stellar spectra contained in data release (DR) 6, the LAMOST archive constitutes a real treasure trove for researchers. The present study uses spectra from LAMOST DR4 (Luo et al. 2018).

### 2.3 ATLAS variable star Data Release One (ATLAS DR1) and the ‘upside-down CBH variables’

Using data from the first two years of operation of the Haleakala telescope (observations up to the end of June 2017), Heinze et al. (2018) published the ATLAS DR1 catalogue. Analysing observations for approximately 142 million stars between declinations of about  $-30^\circ \leq \delta \leq +60^\circ$  in the magnitude range of about  $11 < r < 19$ , they produced a major catalogue containing  $\sim 430,000$  confirmed variable stars (among which are  $\sim 300,000$  new discoveries) and 4.7 million candidate variable stars. The observations consisted of four to six 30-s exposures of each field per night; the provided data sets boast a median time span of about 620 d, the median number of observations is  $N = 208$  (Heinze et al. 2018). Subsequent data releases are planned, which are expected to greatly enhance the number of identified variables and available measurements.

Heinze et al. (2018) calculated an extensive set of 169 variability features for each object, 70 of which were employed as input for sorting the stars into broad, astrophysically meaningful variability classes based on light curve morphology, such as CBF = ‘Close binary, full period’; CBH = ‘Close binary, half period’; MIRA = ‘High-amplitude, long-period red variable’; PULSE = ‘Pulsating variable’ etc. A complete overview of the variability classes is provided in Table 2 of Heinze et al. (2018).

In the context of the present study, the class of CBH = ‘Close binary, half period’ is of importance, which consists of close eclipsing binaries for which a period equal to half the true orbital period was selected by the employed period search algorithm. In analogy to this group of objects, and in want of a better expression, Heinze et al. (2018) coined the term ud-CBH variables to refer to a particular set of light curves that look almost exactly like the inverted light curves of CBH stars – that is, instead of the minima (eclipses) in the light curves of CBH binaries, they show narrow symmetrical maxima (cf. Figure 1, upper panels). About 70 such objects were manually identified, most of which were sorted into the PULSE class by the classification algorithm. However, the authors note that many more can probably be found in the final catalogue.

Heinze et al. (2018) briefly consider the astrophysical nature of

<sup>2</sup> Guo Shou Jing (1231–1316) was a Chinese astronomer, hydraulic engineer, mathematician, and politician of the Yuan Dynasty.

<sup>3</sup> <http://www.lamost.org>

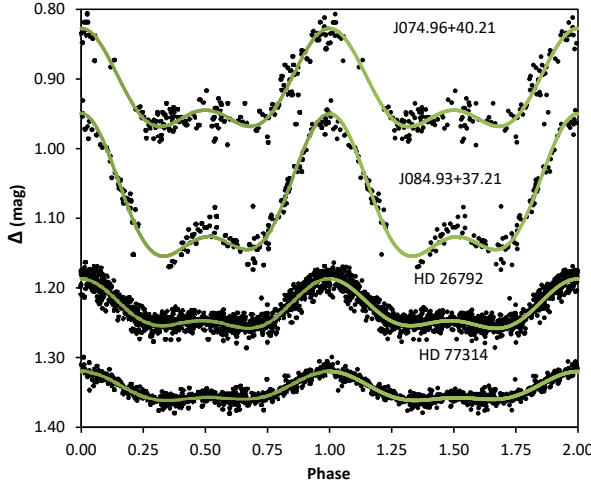


**Figure 1.** Phase plots of (from top to bottom) the ‘upside-down CBH variables’ ATO J074.9570+40.2063 and ATO J084.9321+37.2119, based on ATLAS data, and the known ACV variables HD 77314 and HD 26792, based on MASCARA data. The amplitude of the light variations appears reduced in the filterless MASCARA data.

the ud-CBH variables, which occupy a well-defined region in period-amplitude space (amplitudes of up to 0.2 mag, period distribution peaks around 2 d; cf. Figure 23 of Heinze et al. 2018). In particular, they rule out contact binaries (GCVS-type EW; Samus et al. 2017) and binary stars with strong reflection effects (GCVS-type R) on the grounds of light curve morphology and argue against ‘ordinary’ rotating variables with classical starspots and binary systems with an accreting compact object because of the consistency of the observed light curves. In summary, the authors were unable to properly classify these stars and present them as a potentially new type of (pulsating?) variables, whose astrophysical nature is unclear.

#### 2.4 Motivation and target selection

The present study was conceived after we noticed the strong similarity of the light curves of the ud-CBH variables illustrated in Heinze et al. 2018 (their Figure 23) to the light curves of a certain subset of ACV variables. Unlike stars with classical starspots, these spotted rotators show simple and remarkably consistent light curves that remain stable in shape and amplitude over decades and more (e.g. Hümmerich et al. 2018). As has been expanded upon in Section 1, the light variations of ACV variables are due to the presence of chemical spots. They generally show simple light curves that can be well described by a sine wave and its first harmonic (e.g. North 1984; Mathys & Manfroid 1985; Bernhard et al. 2015a). Depending on the inclination of the rotational axis and the number of spots that come into view during the rotation cycle, most ACVs show either single-wave or double-wave light curves (e.g. Maitzen 1980; Jagelka et al. 2019). In the case of two dominant spots of different sizes or photometric properties on opposing hemispheres of the star, a double-wave light curve with maxima of different heights is to be expected, in agreement with the light curves of the ud-CBH variables. This variability pattern is fairly unique among early-type stars and, according to our experience (Bernhard et al. 2015a,b; Hümmerich et al. 2016), a tell-tale sign of ACV variables. According to the study of Jagelka et al. (2019), roughly one third of ACV variables are expected to show

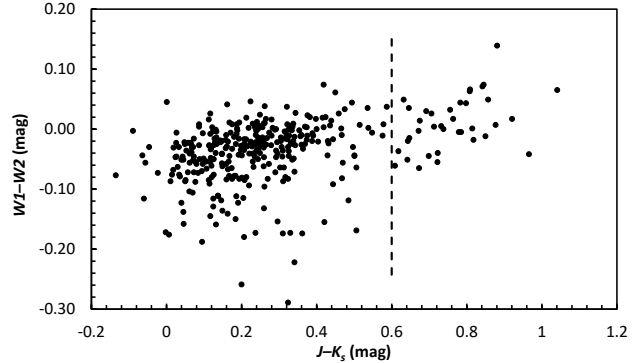


**Figure 2.** Near-/mid-infrared colour-colour diagram of all stars selected via the criteria outlined in Section 2.4. Note the ‘red tail’ of objects with  $(J - K_s) > 0.6$  mag.

double-wave light curves, with half of these stars exhibiting maxima of different height.

Furthermore, the characteristics of the ud-CBH variables given in Heinze et al. (2018) – low-amplitude ( $< 0.2$  mag) variability; periods in the range of about  $1 < P(d) < 5$ , with a peak around 2 d – are in agreement with the majority of ACV variables, which mostly exhibit rotational periods in the above mentioned period range, with a well-known peak around 2 d (e.g. Renson & Manfroid 2009; Bernhard et al. 2015b). A comparison of the light curves of two ud-CBH variables from the list of Heinze et al. (2018) to the light curves of two double-waved ACV variables taken from Bernhard et al. (2020) is provided in Figure 1. While the amplitude of the light variations appears reduced in the filterless data from the Multi-site All-Sky CAmeRA (MASCARA; Snellen et al. 2012; Talens et al. 2017), the general variability pattern is the same. As an initial test of our hypothesis, we investigated the LAMOST DR4 spectra of several ud-CBH stars, which confirmed our suspicion that these objects are indeed mCP (mostly CP2) stars.

For the final target selection process, several considerations had to be taken into account. As ‘ud-CBH stars’ is not one of the final adopted variability classes, these objects cannot be simply queried via the interface to the ATLAS DR1 catalogue.<sup>4</sup> Heinze et al. (2018) comment that most ud-CBH variables were sorted into the category PULSE by the classification algorithm. Apart from that, we consider the CBH and SINE groups the most promising targets for discovering ACV variables among the remaining variability classes. The SINE group (‘Pure sine was fit with small residuals’) was chosen because most ACV stars (roughly 50 % of the sample of Jagelka et al. 2019) show symmetric single-wave light curves that can be well fitted by a sine wave. All other variability groups were ruled out as primary targets on grounds of the covered period and amplitude ranges, the occurrence of multiple periods, irregular variability, or, as ACV variables show remarkably stable light curves, the indication of large residuals to the sine fit (class NSINE = ‘Noisy sine: pure sine was fit, but residuals are large or nonrandom’).

On grounds of these considerations, and after some initial testing regarding the feasibility of our intended approach, we decided to investigate objects from the PULSE, CBH, and SINE groups with the following requirements: (i)  $0.5 < P(d) < 10$ , (ii) peak-to-peak vari-

<sup>4</sup> More information on how to query the ALTAS DR1 catalogue is available at <https://archive.stsci.edu/prepds/atlas-var/>.

ability amplitude in the  $c$  band of  $\text{amp}(c) < 0.3$  mag, and (iii) phase offset  $\phi_2 - \phi_1$  of the first two Fourier terms between  $60^\circ$  and  $110^\circ$ . The imposed cuts form a compromise between an effective identification of mCP stars and the need to keep the sample down to a manageable size. The period (i) and phase offset (iii) requirements were enforced to exclude  $\delta$  Scuti (GCVS-type DSCT) stars or other short period pulsators and W UMa variables. Item (iii) was chosen according to the results of Heinze et al. (2018), who find that most ud-CBH stars have phase offsets near  $90^\circ$  (cf. in particular their Figure 23). We note that while there exist mCP stars with rotation periods in excess of the chosen limit, their incidence drops significantly towards longer rotational periods (e.g. Renson & Manfroid 2009); more importantly, the number of suitable light curves in the ATLAS DR1 catalogue diminishes rapidly at  $P > 10$  d. The peak-to-peak variability cut-off (ii) was set deliberately high in order not to per se exclude any high-amplitude ACV variables. Although most ACV stars show amplitudes smaller than 0.2 mag ( $V$ ), we noticed several stars with amplitudes approaching this limit in the  $c$  band (cf. Figure 1).

Frequency spectra of all objects selected via these criteria were calculated using PERIOD04 (Lenz & Breger 2005). Light curves and frequency spectra were then visually inspected. Obviously multiperiodic objects, such as slowly pulsating B (GCVS-type SPB) stars and  $\gamma$  Doradus (GCVS-type GDOR) variables, were discarded; mono-periodic objects (that is, objects with frequency spectra indicative of a single significant frequency or a single significant frequency plus corresponding harmonics) with stable light curves typical of ACV variables were chosen for further consideration.

Although spot configurations in late-type stars are much more unstable, we expect contamination by late-type rotational variables such as BY Draconis (GCVS-type BY) or RS Canum Venaticorum (GCVS-type RS) stars that, at least in the investigated time-span, did not show significant changes in spot sizes and distribution and therefore exhibited appreciably stable light curves. For this reason, as an initial check, the remaining objects were plotted in a near-/mid-infrared colour-colour diagram (Figure 2) in order to identify red stars. To this end, we employed photometry from the 2MASS (Skrutskie et al. 2006) and WISE (Wright et al. 2010) catalogues. Considering the faintness of the investigated objects and the unknown amount of reddening in the line-of-sight, this will only have a limited predictive value as regards the intrinsic colours of the stars. However, there is an obvious red tail of objects with  $(J - K_s) > 0.6$  mag, which likely corresponds to late-type rotational variables. For several of these objects, LAMOST DR4 spectra are available, which indeed confirmed this assumption. Three exemplary spectra are shown in Figure 3. As expected, all objects show signs of increased chromospheric activity, which is typical of late-type rotational variables. We therefore felt justified in excluding objects with  $(J - K_s) > 0.6$  mag from further consideration.

264 stars passed the imposed selection criteria, which, for convenience, are hereafter referred to as the 'final sample'. The full list of parameters for these objects is provided in Table A1 in the Appendix (Section A). A sample page illustrating the light curves of the first 16 stars from our sample is also provided in the Appendix (Figure C1). The full set of light curves is obtainable online.

### 3 SPECTRAL CLASSIFICATION

The final sample was cross-matched with the LAMOST DR4 VizieR online catalogue<sup>5</sup> (Luo et al. 2018), requiring  $S/N \geq 25$  in the Sloan  $g$  band. In this manner, spectra for 62 stars could be procured. If more than one spectrum was available for a single object, only the spectrum with the highest  $g$  band  $S/N$  was considered.

Spectral classification was performed in the framework of the refined MK classification system following the methodology outlined in Gray & Garrison (1987, 1989a,b); Garrison & Gray (1994) and Gray & Corbally (2009). For a precise classification and to identify peculiarities, the blue-violet (3800–4600 Å) spectral region was compared visually to, and overlaid with, MK standard star spectra and a set of synthetic spectra.

The standard star spectra were taken from the *libr18* and *libnor36* libraries that are distributed with the MKCLASS code<sup>6</sup>, a computer program written to classify stellar spectra on the MK system (Gray & Corbally 2014), and the *liblamost* library, which is a preliminary set of suitable LAMOST spectra compiled by Hünnerich et al. (2020). The synthetic spectra were calculated using the program SPECTRUM<sup>7</sup> (Gray & Corbally 1994) and ATLAS9 model atmospheres (Castelli & Kurucz 2003), assuming  $\log g = 4.0$ ,  $[M/H] = 0.0$  and a microturbulent velocity of  $2 \text{ km s}^{-1}$ . The spectra were then subsequently smoothed to a resolution of  $3.0 \text{ \AA}$  to provide a good match to the LAMOST spectra.

mCP stars exhibit several peculiarities related to traditional classification criteria, which need to be taken into account when assigning a spectral type to these objects. They often show weak, unusually broad or otherwise peculiar Ca II K line profiles, weak Mg II 4481 Å lines and are markedly He deficient (Gray & Corbally 2009; Ghazaryan et al. 2018). The latter characteristic resulted in the classification of many of the hotter (late B-type) mCP stars as A-type stars because of the lack of, or the occurrence of only very weak, He I lines in their spectra (Gray & Corbally 2009). Furthermore, mCP stars generally show enhanced and peculiar metallic lines. In general, therefore, the hydrogen-line profile is the most accurate indicator of the actual temperature of these objects (Gray & Corbally 2009).

We have determined spectral types based on the Ca II K line strength (the k-line type) and the hydrogen-line profile (the h-line type) (Osawa 1965). Spectral types based on the strength of the He I lines were not determined for all stars but only in the case of the He-weak/CP4 stars and where they were unambiguously visible in the spectra. Most late B-type stars in our sample appear noticeably He weak.

The metallic lines of most mCP stars are so peculiar that they cannot be used for luminosity classification. Luminosity types, therefore, were based on the wings of the hydrogen lines. In this respect, it is important to note that a considerable number of mCP stars shows narrow or unusual hydrogen-line profiles (e.g. Faraggiana 1987; Garrison & Gray 1994; Ghazaryan et al. 2018) which are best matched by the profiles of high-luminosity objects like giants or even bright giants (luminosity classes III and II, respectively). This also holds true for many stars of our sample, although, apart from the hydrogen-line profile, other high-luminosity indicators are mostly absent from their spectra. It is well known that the vast majority of mCP stars are in fact main-sequence objects (Netopil et al. 2017 and references therein) and our results from the colour-magnitude diagram (CMD) (Section 5) fully support this finding. Non-LTE effects may be at the root of

<sup>5</sup> <http://cdsarc.u-strasbg.fr/viz-bin/cat/V/153>

<sup>6</sup> <http://www.appstate.edu/~grayro/mkclass/>

<sup>7</sup> <http://www.appstate.edu/~grayro/spectrum/spectrum.html>

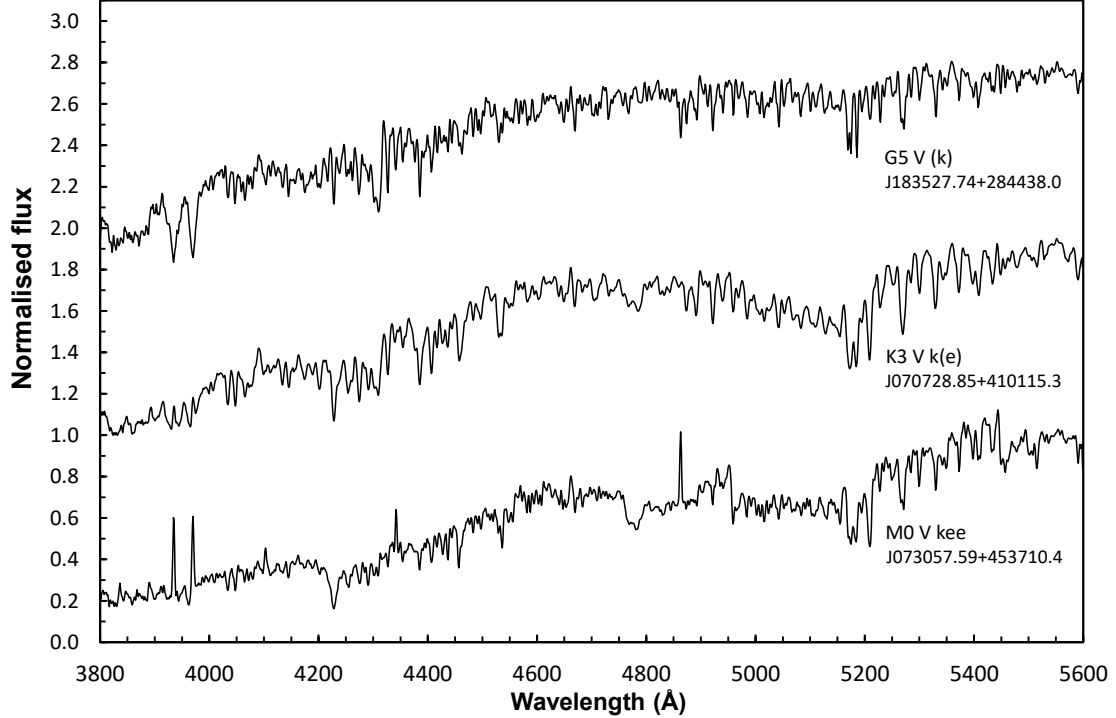


**Figure 3.** Spectra of late-type rotational variables from the ‘red tail’ with  $(J - K_s) > 0.6$  mag, showing signs of increased chromospheric activity. Identifiers and spectral types (derived in this study) are indicated in the plot. The spectrum of J070728.85+410115 shows emission in the H alpha line (not shown in the plot).

this obvious discrepancy between the luminosities derived from the hydrogen-line profiles and other indicators (Garrison & Gray 1994). Perhaps the influence of the strong magnetic fields results in unusual atmospheric structures; however, this remains as yet unsolved.

Main chemical peculiarities are given in order of importance. Parentheses and a double pair of parentheses have been employed to indicate that a peculiarity is, respectively, weakly or only marginally present (Gray & Garrison 1987, 1989a,b; Garrison & Gray 1994). Likewise, the notation “metallic lines” is used to indicate a faint background of metallic lines due to other atomic species than iron, titanium, or their ions (Gray & Garrison 1987). This notation may also appear in parentheses or a double pair of parentheses.

For several objects, only spectra of low S/N ( $S/N < 40$ ) are available. Spectral types based on these spectra should be regarded as estimates only. For instance, the difference between the hydrogen-line profiles of a B8 III star and a B5 V star gets blurred in low S/N spectra (Garrison & Gray 1994). As mCP stars often show weak He lines, this leads to corresponding uncertainties in the spectral classification.

Example spectra are provided in Figure 4; final spectral types and remarks are presented in Table 1. We also investigated the 4800–5600 Å spectral region to check for the presence and morphology of the flux depression around 5200 Å, which is a characteristic of mCP stars (Kodaira 1969; Kupka et al. 2003; Khan & Shulyak 2007) and readily visible at LAMOST resolution (Hümmerich et al. 2020). Unless indicated otherwise in the remarks, all objects show a clearly visible 5200 Å feature in their spectra, as expected.

Nine of the spectroscopically confirmed mCP stars are contained in the sample of Hümmerich et al. (2020); the remaining 54 stars are here presented as mCP stars for the first time. Our classifications agree well with the automatically derived classifications from the aforementioned study. Hümmerich et al. (2020) did not specify k-line types for all objects; however, the h-line types, the most important temperature-type criterion in mCP stars, agree very well: the differences amount to 0.0 spectral subclasses in the case of six objects, 0.5 spectral subclasses in the case of two stars, and 2.0 spectral subclasses in the case of one star (one spectral subclass being the difference between, for instance, A0 and A1). The main spectral peculiarities have been correctly identified by Hümmerich et al. (2020); using manual classification, we can in some cases add weak peculiarities that have been missed by their code and, in two cases, are able to resolve the generic ‘bl4077’ (strong 4077 Å blend) and ‘bl4130’ (strong 4130 Å blend) types into their contributing ions. For instance, in the case of J072338.12+003848.5, ‘bl4077’ resolves into Si II 4076 Å and Sr II 4077 Å, and ‘bl4130’ into Si II 4128–30 Å and Eu II 4130 Å. Classifications from Hümmerich et al. (2020), where available, are also provided in Table 1.

#### 4 MAGNITUDE, PERIOD AND SPACE DISTRIBUTION

The upper panel of Figure 5 illustrates the histogram of the  $G$  magnitudes of the spectroscopically confirmed mCP stars ( $N = 62$ ) and the mCP star candidates ( $N = 202$ ) of our final sample. The magnitude

**Table 1.** Spectral types of the mCP stars identified in the present study. The columns denote: (1) ATLAS object identifier. (2) LAMOST identifier. (3) Sloan *g* band S/N ratio of the analysed spectrum. (4) Spectral type, as derived in this study. (5) Remark. 'H20' denotes spectral types from the study of Hümmerich et al. (2020).

(1)	(2)	(3)	(4)	(5)
ID_ATO	ID_LAMOST	S/N <i>g</i>	SpT_final	remark
J046.2665+57.4649	J030503.98+572753.7	33	kA0 hB7 HeB8 V Si(Sr)	no 5200 Å flux depression visible
J046.9585+53.9453	J030750.05+535643.2	98	kA0 hA0: III-IV (Si)	$\lambda$ 4481 weak
J047.5021+53.3159	J031000.50+531857.3	30	kA1 hA3 III SiCrEu	
J050.9303+44.3793	J032343.27+442245.4	108	kA0 hA0 II EuSi	$\lambda$ 4481 weak; H20: A0 Ib-II EuSi
J053.2447+44.4347	J032528.73+442605.0	69	kB9.5 hB9 III SiEuCr	$\lambda$ 44172-9 strong
J057.4910+58.7724	J034957.85+584620.8	57	kA0 hB9.5 III Si(Cr)Eu	$\lambda$ 4481 weak
J060.7275+46.2448	J040254.59+461441.4	45	kA1 hB9: II: SiEuSr	$\lambda$ 4481 weak
J060.7480+45.3172	J040259.53+451902.0	113	kA1 hA1 III SiEu((Cr))	$\lambda$ 4481 weak
J063.5805+46.9075	J041419.32+465427.1	42	knA1 hA5 III EuCrSr(Si)	$\lambda$ 4481 weak
J064.2611+46.2848	J041702.66+461705.5	65	kA0 hA0 III-IV Si	$\lambda$ 4481 weak
J065.7038+47.6938	J042248.93+474138.0	308	kA0 hA0 II EuSiCr	$\lambda$ 4481 weak; H20: A0 II Eu
J066.9854+44.3739	J042756.51+442226.2	67	kB9.5 hB8 IV Si	$\lambda$ 4481 weak
J067.4887+38.9535	J042957.29+385712.5	58	knB9 hB5 V Si	
J072.5642+39.5294	J045015.40+393146.0	78	kA1 hA5 III SiCr	
J074.4268+43.8711	J045742.44+435216.0	30	kA0 hA5 III-IV SiEuSr	$\lambda$ 4481 weak
J074.9570+40.2063	J045949.68+401222.8	83	kA0 hB9 III-IV SiEu	$\lambda$ 4481 broad and shallow
J074.9889+42.2979	J045957.34+421752.6	31	kA0 hB9 III SiEuCr	
J076.4023+45.6101	J050536.57+453636.6	59	kA1 hB9 III EuSi	Eu very strong; $\lambda$ 4481 broad and shallow
J077.0867+36.5911	J050820.81+363528.0	41	kB9.5 hB8 V (Si) ((metallic lines))	very weak 5200 Å flux depression
J081.9629+42.4325	J052751.11+422557.3	92	kB9.5 hB9.5 III Si	$\lambda$ 4481 weak
J082.5579+33.1925	J053013.91+331133.3	31	kA0 hB9: III: SiCr:Eu:	$\lambda$ 4481 weak
J082.6115+29.6992	J053026.78+294157.2	84	kA0 hB9 III Si	$\lambda$ 4481 weak
J082.6322+21.1693	J053031.74+211009.4	103	kB9 hB7 HeB9 V ((metallic lines))	
J084.9321+37.2119	J053943.72+371243.0	59	knA0 hB9 V SiEu((Cr))	$\lambda$ 4481 broad and shallow
J086.1147+31.8873	J054427.54+315314.3	28	kA1 hB9 IV Si:Cr:Eu:	
J086.1972+24.3919	J054447.34+242331.1	52	kB9 hB7 HeB8 V ((Si)) (metallic lines)	
J086.3082+11.2506	J054513.97+111502.4	232	kB8 hB8 V Si	$\lambda$ 4481 weak
J086.4762+23.3391	J054554.30+232021.0	47	kA0 hB9 III SrCrEuSr	$\lambda$ 4481 slightly weak
J086.5553+40.4840	J054613.28+402902.7	98	kA0 hB9 IV Si(SrCr)	$\lambda$ 4481 weak
J087.1757+29.1833	J054842.18+291059.9	35	kA0 hB9: V: SiEuCr	$\lambda$ 4481 weak
J087.2218+29.4548	J054853.23+292717.3	26	kB9 hA0: III: SiCrEu	$\lambda$ 4481 weak
J088.2315+38.6528	J055255.56+383910.1	47	kB9 hB7 HeB9 V Si (metallic lines)	$\lambda$ 4481 weak
J090.0237+21.9017	J060005.70+215406.3	40	kA0 hB9 V CrSiEu	
J090.7455+31.0548	J060258.92+310317.1	37	kB9 hB9: II: SiCrSr	$\lambda$ 4481 weak
J091.1746+24.8696	J060441.92+245210.8	26	kB9: hB9: III: Si	$\lambda$ 4481 weak
J091.9664+24.5688	J060751.94+243407.9	95	kB9 hB5 HeB9 IV (Si) (metallic lines)	
J093.7415+41.4780	J061457.97+412840.8	112	kA1 hA5 V Eu	$\lambda$ 44172-9 strong
J093.9930+13.8659	J061558.32+135157.3	148	kB9 hB5 HeB9 V (SiSr)Ti?	H20: B5 III-IV bl4130 (He-wk)
J094.3323+15.5243	J061719.74+153127.5	86	kB9.5 hB7 HeB9 V Si	
J094.7507+19.5193	J061900.18+193109.6	76	knA0 hA0: II-III SiEuCr	$\lambda$ 4481 weak
J095.0108+01.8715	J062002.59+015217.4	41	kA0 hB9 IV SiCrSrEu	$\lambda$ 4481 weak
J095.4959+23.6564	J062159.02+233923.1	42	knB9 hB8 HeB9 V SiCr	
J096.8934+14.9451	J062734.41+145642.6	37	kA1 hA3: III: Cr:Si:	$\lambda$ 4481 weak
J097.1763+16.4813	J062842.31+162852.9	168	kB9.5 hB9.5 III EuSi((Cr))	$\lambda$ 4481 weak; H20: B9.5 II-III EuSi
J097.4242+24.5808	J062941.80+243450.9	155	kB9 hB7 HeB8 V	
J097.6873+03.0070	J063044.96+030025.3	61	kB9 hB7 HeB9: V	
J098.5904+17.0987	J063421.70+170555.6	83	knA0 hB9 III Si	$\lambda$ 4481 weak
J098.6389+19.1051	J063433.34+190618.6	26	kA0 hB8 IV SiCr:Eu:	$\lambda$ 4481 weak
J099.0745+18.8221	J063617.89+184919.6	28	kB9 hB9 IV SiEuCr	
J099.6853+17.3396	J063844.48+172022.5	162	kA0 hB9 III Si(Sr)((Cr))	$\lambda$ 4481 weak; H20: B9 III-IV Si
J100.3063+00.9026	J064113.52+005409.4	43	kA0 hB8 IV SiCr	$\lambda$ 4481 weak
J101.1743+21.6307	J064441.84+213750.5	132	kA0 hA0 II EuSi((Cr))	$\lambda$ 4481 weak; H20: A0 II EuSi
J101.3758+01.7599	J064530.19+014535.8	97	kB9 hB8 V SiEu((Cr))	$\lambda$ 4481 weak
J103.3079+10.5510	J065313.89+103303.3	119	kA0 hA0 III EuSi	$\lambda$ 4481 weak; H20: kA0hA2mA5 Eu
J103.8576-00.4954	J065525.82-002943.4	71	kA0 hB5 V (metallic lines)	
J105.0327+06.1169	J070007.86+060701.0	50	kA1 hA1 II: EuCrSi	$\lambda$ 4481 weak
J106.4471-03.7806	J070547.31-034650.2	80	kB9.5 hB9 III: (metallic lines)	
J106.5580+18.8987	J070613.94+185355.6	63	kA0 hB9 III Si	H20: B9.5 II-III Si
J110.2675-03.2520	J072104.20-031507.4	142	kA0 hB9 III SiSrEu	$\lambda$ 4481 weak; H20: B9.5 II-III bl4077 bl4130
J110.9088+00.6468	J072338.12+003848.5	94	knB9 hB9 IV-V SiSrCrEu	$\lambda$ 4481 weak; very broad Ca II K line blend
J306.9801+45.3863	J202755.24+452311.0	99	kA0 hB9 IV Si(EuSr)	$\lambda$ 4481 weak
J350.3833+56.4514	J232132.00+562705.2	57	kA0 hA3 III EuSi	$\lambda$ 4481 weak

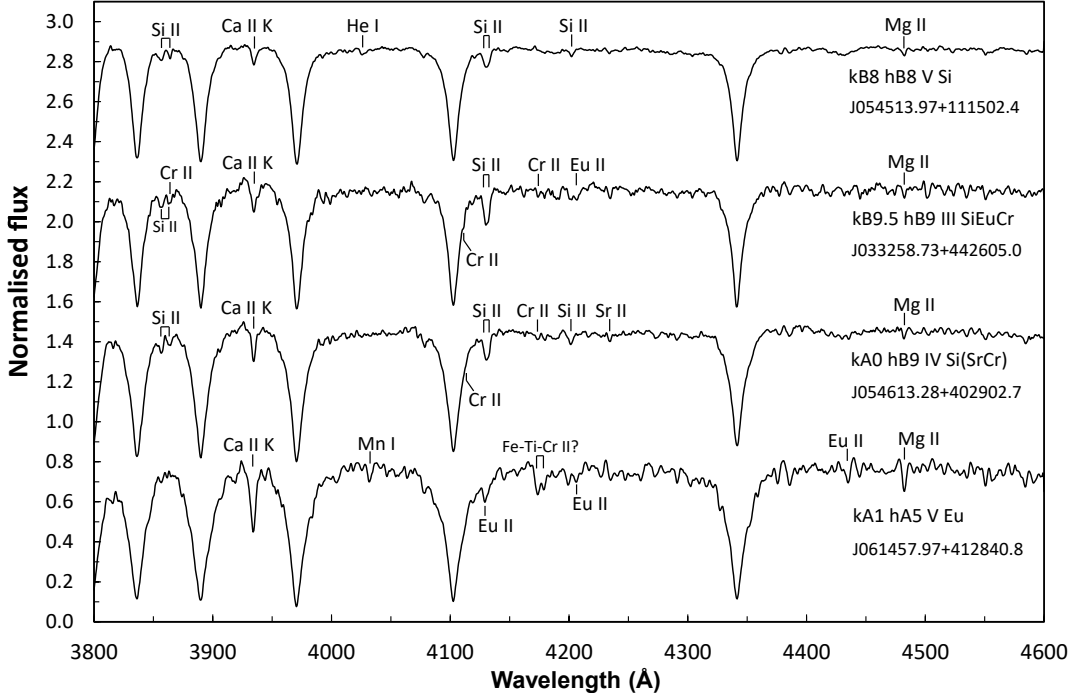


**Figure 4.** Blue-violet region of the LAMOST DR4 spectra of (from top to bottom) the CP2 stars LAMOST J054513.97+111502.4 (ATO J086.3082+11.2506), LAMOST J033258.73+442605.0 (ATO J053.2447+44.4347), LAMOST J054613.28+402902.7 (ATO J086.5553+40.4840), and LAMOST J061457.97+412840.8 (ATO J093.7415+41.4780). Some prominent lines of interest are identified.

distribution peaks around 14th magnitude. For comparison, the stars in the catalogues of [Renson & Manfroid \(2009\)](#) and [Hümmerich et al. \(2020\)](#) peak at 9th magnitude and between 11th and 12th magnitude, respectively. With this work, we therefore extend the search for new mCP stars to even fainter magnitudes.

The period histogram is presented in the lower panel of Figure 5. All periods were extracted from [Heinze et al. \(2018\)](#) and are presented, together with other parameters, in Table A1. The period distribution is fully in agreement with the observed rotational periods of mCP stars, which generally cluster at around a period value of 2 days (e.g. [Renson & Manfroid 2009](#); [Bernhard et al. 2015b](#)). We recall the here imposed period cut-off ( $0.5 < P(d) < 10$ ), which was chosen to exclude short-period pulsators and because the number of suitable light curves in the ATLAS DR1 catalogue diminishes rapidly at  $P > 10$  d (cf. Section 2.4). Any mCP stars with rotation periods longer than 10 days will therefore have been missed by our approach.

The coordinates in the Galactic [XYZ] plane were obtained via the conversion of spherical Galactic coordinates (latitude and longitude) to Cartesian coordinates using the distance  $d$  from [Bailer-Jones et al. \(2021\)](#). Only objects with absolute parallax errors less than 25 % ( $N = 257$ ) were considered. The positive X-axis is towards the Galactic centre, the positive Y-axis is in the direction of the Galactic rotation, and the positive Z-axis is towards the north Galactic pole.

Our results are shown in the Appendix in Figure B1. Most sample stars classify as either members of the thin disk (scale height of 350 pc) or the thick disk (1200 pc). The corresponding scale heights

were adopted from [Ojha \(2001\)](#) and [Aumer & Binney \(2017\)](#). Interestingly, four stars (ATO J265.2024+10.6314, ATO J072.9129-07.0638, ATO J005.5419+15.5369, and ATO J310.1614-15.1051) are situated more than 1200 pc above or below the [XY] plane and thus qualify as members of the halo population. This is of considerable interest as only very few halo CP2 stars are known ([Hümmerich et al. 2020](#)).

## 5 MASS AND AGE DISTRIBUTION

For generating a colour-magnitude diagram (CMD), we employed the homogeneous Gaia DR2 photometry of [Arenou et al. \(2018\)](#) and the photogeometric distances of [Bailer-Jones et al. \(2021\)](#), which are based on the Gaia EDR3 ([Riello et al. 2021](#)). As most of our sample stars are members of the Galactic disk and situated within a mean distance of 2500 pc from the Sun, interstellar reddening is significant and needs to be taken into account. To estimate the absorption in the line-of-sight, we interpolated the reddening map of [Green et al. \(2018\)](#) using the Gaia EDR3 photogeometric distances. Reddening values were transformed using the relations

$$E(B-V) = 0.76E(BP-RP) = 0.40A_G, \quad (1)$$

which take into account the coefficients listed in [Green et al. \(2018\)](#).

The Gaia DR2 photometry was corrected as suggested by [Maíz Apellániz & Weiler \(2018\)](#). The PARSEC isochrones ([Bressan et al. 2012](#)) for solar metallicity  $[Z] = 0.02$  dex and the filter curves from

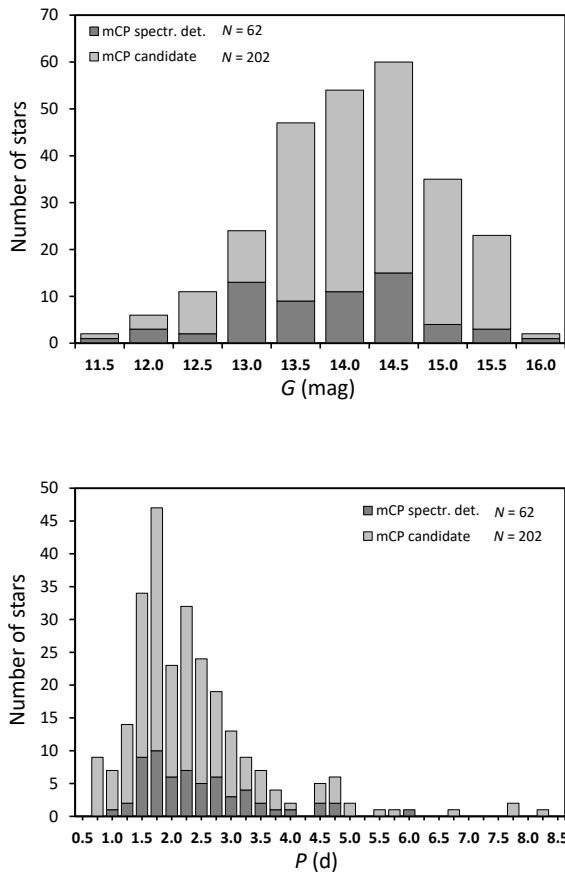


**Figure 5.** Histograms of the  $G$  magnitudes (upper panel) and photometric periods (lower panel) of the spectroscopically confirmed mCP stars ( $N = 62$ ) and the mCP star candidates ( $N = 202$ ) of our final sample.

Maíz Apellániz & Weiler (2018) were used for further analysis. For the estimation of the stellar mass and logarithmic ages, the Stellar Isochrone Fitting Tool<sup>8</sup> was used, which searches for the best-fit evolutionary track within a model grid box. The four grid points closest to the input value are determined, from which the output parameters are derived by bilinear interpolation following the methodology described by Malkov et al. (2010).

The CMD (Figure 6) shows that our sample contains no young stars near the zero-age main sequence (ZAMS). This allowed a corresponding restriction of the tracks in the models to increase the accuracy of the estimates. Parameters could not be determined for five stars of our sample (ATO J076.1702+08.2581, ATO J115.0928-10.6198, ATO J117.8237-09.5101, ATO J308.7048+45.8077, and ATO J321.3283+53.8969) because they did not fit into the grid of models.

Figure 7 shows the mass and age distribution of our sample stars, the complete list of parameters is given in Appendix A. Derived masses range from  $1.4 M_{\odot}$  (a spectral type of about F3) to  $5 M_{\odot}$  (B5). However, half of our sample stars have masses between 2 and  $2.4 M_{\odot}$  (A2 to B9), which is in line with the spectral classifications presented in Section 3. There is only a single outlier with a mass of

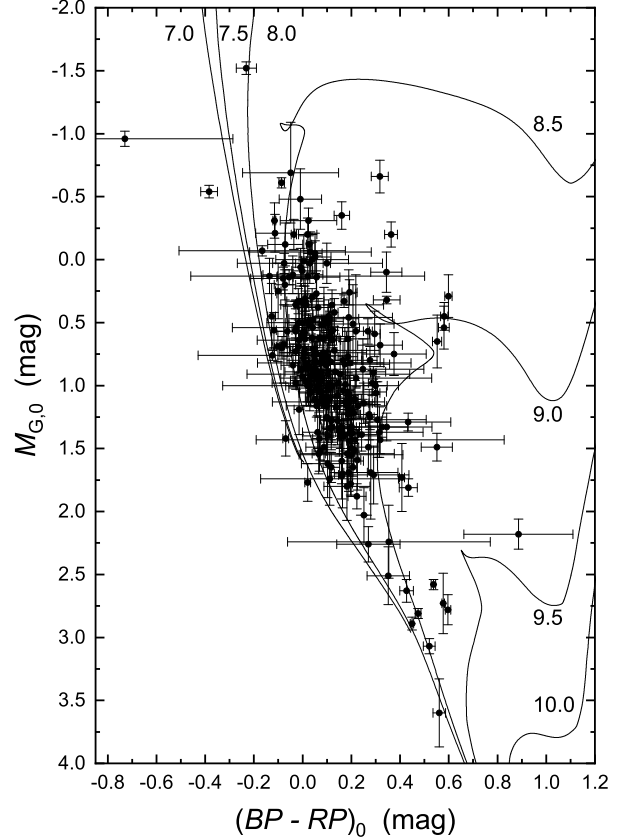


**Figure 6.**  $(BP - RP)_0$  versus  $M_{G,0}$  diagram of our sample stars. Also indicated are PARSEC isochrones for solar metallicity  $[Z] = 0.02$  dex. Ages are given in logarithmic units of years.

$4.8 M_{\odot}$ . The derived ages are in agreement with the results from the CMD; the vast majority of our sample stars are main-sequence objects situated rather close to the terminal-age main sequence (TAMS).

## 6 CONCLUSIONS

Instigated by the similarity of the light curves, periods and amplitudes of the ‘upside-down CBH variables’ shown in Heinze et al. (2018) to the parameters of the class of ACV variables, we carried out a search for ACV variables in the ATLAS DR1 catalogue. Our main results are summarised in the following.

- Using suitable selection criteria ( $0.5 < P(d) < 10$ ;  $\text{amp}(c) < 0.3$  mag; phase offset  $\phi_2 - \phi_1$  of the first two Fourier terms between  $60^\circ$  and  $110^\circ$ ; stable light curves; monoperiodicity; suitable near-/mid-infrared colours), we identified 264 candidate ACV variables.

- 62 of these objects could be spectroscopically confirmed as mCP stars with LAMOST spectra and were classified on the MK system. Nine of these objects are included in the sample of Hümerich et al. (2020); the other 54 stars are new discoveries. The remaining 202 stars are here presented as ACV star candidates that require further observations.

- We present basic stellar parameters for all sample stars. Derived

<sup>8</sup> <https://github.com/Johaney-s/StIFT>

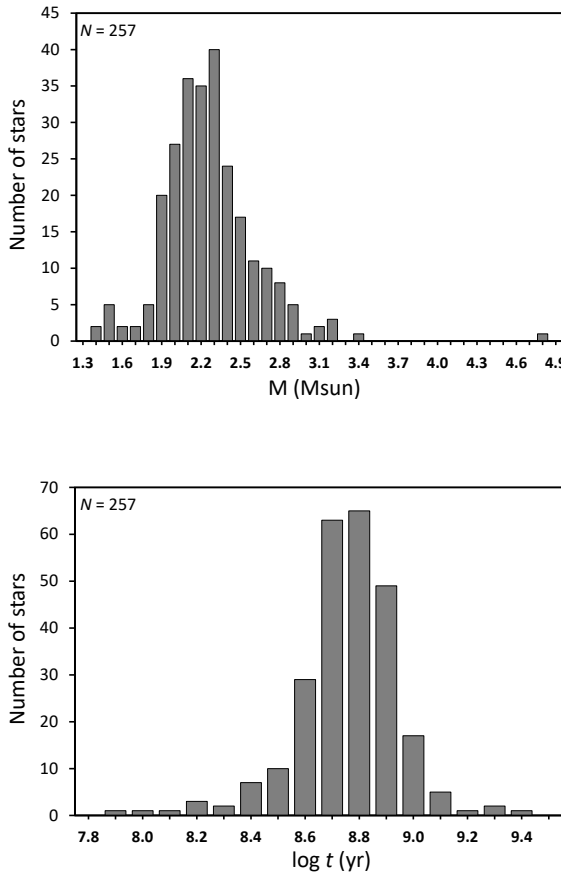


**Figure 7.** Histograms of the estimated masses (upper panel) and the logarithmic ages (lower panel) of our sample stars.

masses range from  $1.4 M_{\odot}$  to  $5 M_{\odot}$ , with half our sample stars being situated in the range from  $2 M_{\odot}$  to  $2.4 M_{\odot}$ . These results are in good agreement with our spectral classifications. As expected, the majority of our sample stars are main-sequence objects.

- Most of our sample stars are members of the thin and thick disk. Four objects (ATO J265.2024+10.6314, ATO J072.9129-07.0638, ATO J005.5419+15.5369, and ATO J310.1614-15.1051) classify as members of the halo population.
- With a peak magnitude distribution at around 14th magnitude, the here presented mCP stars and candidates are situated at the faint end of the known Galactic mCP star population.

While ACV variables have been included into automated classification routines with good success in the past (e.g. Sitek & Pojmański 2014), several of the more recent, massive variability catalogues, such as Heinze et al. (2018) and Chen et al. (2020), do not specifically consider this class of variable stars. Nevertheless, ACV variables are characterised by a distinct set of parameters in period, amplitude and colour spaces as well as concerning their light curve morphology (monoperiodicity, light curve stability, characteristic phase offset), and should therefore be well suited for automated classification attempts.

Our study shows that a dedicated search for ACV variables in catalogues that do not consider this class is a good starting point for the identification of further members of this group of variables.

In general, we expect that the advent of high-precision, multi-colour and spectroscopic surveys will open up a multitude of possibilities to identify new ACV variables, and hence increase the sample size of known mCP stars, in the future.

## ACKNOWLEDGEMENTS

We thank the referee for his/her comments that helped to improve the paper. EP acknowledges support by the Erasmus+ programme of the European Union under grant number 2020-1-CZ01-KA203-078200. The Guo Shou Jing Telescope (the Large Sky Area Multi-Object Fiber Spectroscopic Telescope, LAMOST) is a National Major Scientific Project built by the Chinese Academy of Sciences. Funding for the project has been provided by the National Development and Reform Commission. LAMOST is operated and managed by National Astronomical Observatories, Chinese Academy of Sciences. This work presents results from the European Space Agency (ESA) space mission Gaia. Gaia data are being processed by the Gaia Data Processing and Analysis Consortium (DPAC). Funding for the DPAC is provided by national institutions, in particular the institutions participating in the Gaia MultiLateral Agreement (MLA). The Gaia mission website is <https://www.cosmos.esa.int/gaia>. The Gaia archive website is <https://archives.esac.esa.int/gaia>.

## DATA AVAILABILITY

The data underlying this article will be shared on reasonable request to the corresponding author.

## REFERENCES

- Arenou F., et al., 2018, *A&A*, **616**, A17  
 Aumer M., Binney J., 2017, *MNRAS*, **470**, 2113  
 Bailer-Jones C. A. L., Rybizki J., Fouesneau M., Demleitner M., Andrae R., 2021, *AJ*, **161**, 147  
 Bernhard K., Hümmerich S., Paunzen E., 2015a, *Astronomische Nachrichten*, **336**, 981  
 Bernhard K., Hümmerich S., Otero S., Paunzen E., 2015b, *A&A*, **581**, A138  
 Bernhard K., Hümmerich S., Paunzen E., 2020, *MNRAS*, **493**, 3293  
 Bowman D. M., Buyschaert B., Neiner C., Pápics P. I., Oksala M. E., Aerts C., 2018, *A&A*, **616**, A77  
 Bressan A., Marigo P., Girardi L., Salasnich B., Dal Cero C., Rubele S., Nanni A., 2012, *MNRAS*, **427**, 127  
 Castelli F., Kurucz R. L., 2003, in Piskunov N., Weiss W. W., Gray D. F., eds, IAU Symposium Vol. 210, Modelling of Stellar Atmospheres. p. A20 ([arXiv:astro-ph/0405087](https://arxiv.org/abs/astro-ph/0405087))  
 Chen X., Wang S., Deng L., de Grijts R., Yang M., Tian H., 2020, *ApJS*, **249**, 18  
 Cui X.-Q., et al., 2012, Research in Astronomy and Astrophysics, **12**, 1197  
 David-Uraz A., et al., 2019, *Monthly Notices of the Royal Astronomical Society*, **487**, 304  
 Djorgovski S. G., Mahabal A., Drake A., Graham M., Donalek C., 2013, Sky Surveys. p. 223, doi:[10.1007/978-94-007-5618-2\\_5](https://doi.org/10.1007/978-94-007-5618-2_5)  
 Faraggiana R., 1987, *Ap&SS*, **134**, 381  
 Garrison R. F., Gray R. O., 1994, *AJ*, **107**, 1556  
 Ghazaryan S., Alecian G., Hakobyan A. A., 2018, *MNRAS*, **480**, 2953  
 Gray R. O., Corbally C. J., 1994, *AJ*, **107**, 742  
 Gray R. O., Corbally C. J., 2009, Stellar Spectral Classification  
 Gray R. O., Corbally C. J., 2014, *The Astronomical Journal*, **147**, 80  
 Gray R. O., Garrison R. F., 1987, *ApJS*, **65**, 581  
 Gray R. O., Garrison R. F., 1989a, *ApJS*, **69**, 301  
 Gray R. O., Garrison R. F., 1989b, *ApJS*, **70**, 623

- Green G. M., et al., 2018, *MNRAS*, **478**, 651  
 Heinze A. N., et al., 2018, *The Astronomical Journal*, **156**, 241  
 Hümmerich S., Paunzen E., Bernhard K., 2016, *AJ*, **152**, 104  
 Hümmerich S., et al., 2018, *A&A*, **619**, A98  
 Hümmerich S., Paunzen E., Bernhard K., 2020, *A&A*, **640**, A40  
 Jagelka M., Mikulášek Z., Hümmerich S., Paunzen E., 2019, *A&A*, **622**, A199  
 Khan S. A., Shulyak D. V., 2007, *A&A*, **469**, 1083  
 Kodaira K., 1969, *ApJ*, **157**, L59  
 Kupka F., Paunzen E., Maitzen H. M., 2003, *MNRAS*, **341**, 849  
 Lanz T., Artru M. C., Le Dourneuf M., Hubeny I., 1996, *A&A*, **309**, 218  
 Lenz P., Breger M., 2005, *Communications in Asteroseismology*, **146**, 53  
 Luo A. L., Zhao Y. H., Zhao G., et al. 2018, *VizieR Online Data Catalog*, **5153**, 0  
 Maitzen H. M., 1980, *A&A*, **89**, 230  
 Maíz Apellániz J., Weiler M., 2018, *A&A*, **619**, A180  
 Malkov O. Y., Sichevskij S. G., Kovaleva D. A., 2010, *MNRAS*, **401**, 695  
 Mathys G., Manfroid J., 1985, *A&AS*, **60**, 17  
 Michaud G., 1970, *ApJ*, **160**, 641  
 Netopil M., Paunzen E., Hümmerich S., Bernhard K., 2017, *MNRAS*, **468**, 2745  
 North P., 1984, *A&AS*, **55**, 259  
 Ojha D. K., 2001, *MNRAS*, **322**, 426  
 Osawa K., 1965, *Annals of the Tokyo Astronomical Observatory*, **9**, 121  
 Paunzen E., Maitzen H. M., 1998, *A&AS*, **133**, 1  
 Preston G. W., 1974, *ARA&A*, **12**, 257  
 Renson P., Manfroid J., 2009, *A&A*, **498**, 961  
 Richer J., Michaud G., Turcotte S., 2000, *ApJ*, **529**, 338  
 Riello M., et al., 2021, *A&A*, **649**, A3  
 Samus N. N., Kazarovets E. V., Durlevich O. V., Kireeva N. N., Pastukhova E. N., 2017, *Astronomy Reports*, **61**, 80  
 Shulyak D., Krtička J., Mikulášek Z., Kochukhov O., Lüftinger T., 2010, *A&A*, **524**, A66  
 Sikora J., et al., 2019, *MNRAS*, **487**, 4695  
 Sitek M., Pojmański G., 2014, *Acta Astron.*, **64**, 115  
 Skrutskie M. F., et al., 2006, *AJ*, **131**, 1163  
 Snellen I. A. G., et al., 2012, in *Ground-based and Airborne Telescopes IV*. p. 84440I ([arXiv:1208.4116](https://arxiv.org/abs/1208.4116)), doi:10.1117/12.925178  
 Talens G. J. J., Spronck J. F. P., Lesage A. L., Otten G. P. P. L., Stuik R., Pollacco D., Snellen I. A. G., 2017, *A&A*, **601**, A11  
 Tonry J. L., et al., 2018, *PASP*, **130**, 064505  
 Watson C. L., 2006, *Society for Astronomical Sciences Annual Symposium*, **25**, 47  
 Wright K. T., Fossati L., Netopil M., Paunzen E., Rode-Paunzen M., Bewsher D., Norton A. J., White G. J., 2012, *MNRAS*, **420**, 757  
 Wright E. L., et al., 2010, *AJ*, **140**, 1868  
 Zhao G., Zhao Y.-H., Chu Y.-Q., Jing Y.-P., Deng L.-C., 2012, *Research in Astronomy and Astrophysics*, **12**, 723

## APPENDIX A: ESSENTIAL DATA OF OUR SAMPLE STARS

## APPENDIX B: DISTRIBUTION OF OUR SAMPLE STARS IN THE GALACTIC [XYZ] PLANE

## APPENDIX C: LIGHT CURVES

This section provides a sample page with the light curves of the first 16 stars of our sample, folded with the periods listed in Table A1. The full set of light curves is available online.

This paper has been typeset from a  $\text{\TeX}$ / $\text{\LaTeX}$  file prepared by the author.

**Table A1.** Essential data for our sample stars, sorted by increasing right ascension. The columns denote: (1) ATLAS object identifier. (2) Gaia EDR3 identifier. (3) Right ascension (J2000; Gaia EDR3). (4) Declination (J2000; Gaia EDR3). (5) X coordinate towards the Galactic centre. (6) Y coordinate in direction of Galactic rotation. (7) Z coordinate towards the north Galactic pole. (8) Magnitude in the *G* band (Gaia EDR3). (9) *G* mag error. (10) Rotational period (ATLAS). (11) Median of the photogeometric distance posterior,  $D$  (Gaia EDR3). (12) Distance error. (13) Dereddened colour index ( $BP - RP$ )<sub>0</sub> (Gaia EDR3). (14) Colour index error. (15) Absorption in the *G* band,  $A_G$ . (16) Intrinsic absolute magnitude in the *G* band,  $M_{G0}$ . (17) Absolute magnitude error. (18) Mass. (19) Logarithmic age.

(1)	(2)	(3)	(4)	(5)	(6)	(7)	(8)	(9)	(10)	(11)	(12)	(13)	(14)	(15)	(16)	(17)	(18)	(19)
ID_ATO	ID_EDR3	RA(J2000)	Dec(J2000)	X (kpc)	Y (kpc)	Z (kpc)	$\epsilon_G$ (mag)	$\epsilon_{-G}$ (mag)	$P_{\text{rot}}$ (d)	$D$ (pc)	$\epsilon_D$ (pc)	$\epsilon_{(BP-RP)_0}$ (mag)	$\epsilon_{(BP-RP)_0}$ (mag)	$M_{G0}$ (mag)	$\epsilon_{M_{G0}}$ (mag)	Mass (M <sub>sun</sub> )	Age (Myr)	
(hh mm ss.ss)	(dd mm ss.ss)																	
0005.5419+15.5369	Gaia EDR3 279238859383811456	00 22 10.059	+15 32 13.056	-1.000	+2.401	-2.765	13.5507	0.0039	0.751927	3796	198	+0.581	0.015	0.21	+0.45	0.11	2.16	9.00
010.7230+57.78087	Gaia EDR3 12425310234623688	00 42 53.329	+57 33 41.384	-0.924	+1.491	-0.155	12.8048	0.0038	0.452355	1761	39	-0.003	0.006	1.02	-0.31	0.14	3.19	8.39
010.3939+57.62344	Gaia EDR3 12425310234623688	00 42 53.329	+57 37 28.060	-2.430	+1.711	-0.407	13.9679	0.0030	1.812188	4455	292	-0.116	0.006	1.02	-0.31	0.14	3.19	8.39
0202.5446+57.3828	Gaia EDR3 12876791016632960	01 46 43.217	+56 29 50.893	-2.698	+1.659	-0.188	14.5231	0.0023	2.146555	4170	372	+0.197	0.007	1.31	+0.36	0.05	2.35	8.61
0202.6809+56.4974	Gaia EDR3 3070437878234098012	01 46 04.09	+59 12.049	-1.411	+1.560	-0.087	12.8886	0.0031	0.481781	2105	59	+0.101	0.010	1.02	+0.51	0.05	2.32	8.67
0301.0380+59.216	Gaia EDR3 3070437878234098012	02 11.44.559	+58 35.69.744	-1.281	+1.853	-0.023	14.1779	0.0031	2.475819	2575	120	+0.115	0.017	1.53	+0.38	0.10	2.32	8.78
0302.9773+58.5869	Gaia EDR3 3056811170882656	02 11.44.559	+58 44.15.122	-1.786	+1.312	-0.023	14.0938	0.0030	0.507814	1980	104	+0.115	0.017	1.53	+0.38	0.10	2.32	8.80
0334.4119+58.6875	Gaia EDR3 345879792431720912	02 17.78.366	+53 17.03.874	-1.345	+1.255	-0.023	14.0938	0.0030	0.5023	1822	104	+0.115	0.017	1.53	+0.38	0.10	2.32	8.80
0388.7653+59.5050	Gaia EDR3 650851303179869000	03 53.61.277	+59 35.86.078	-1.621	+1.255	-0.023	14.0938	0.0030	0.5023	1822	104	+0.115	0.017	1.53	+0.38	0.10	2.32	8.80
0398.9359+57.400	Gaia EDR3 4590851303179869000	02 39.15.525	+57 24.03.726	-1.986	+1.847	-0.117	15.0181	0.0032	1.129881	2714	162	+0.195	0.013	1.47	+1.37	0.13	1.99	8.88
0401.523235+57.1887	Gaia EDR3 46079578071772416	02 49.36.079	+57 25.85.859	-2.244	+2.019	-0.123	12.8048	0.0031	1.588903	3021	54	+0.296	0.022	1.52	+0.59	0.18	2.25	8.89
0402.3277+57.1063	Gaia EDR3 46079578071772416	02 49.18.660	+57 26.22.3	-1.979	+1.759	-0.100	15.0568	0.0030	0.679799	2647	176	+0.062	0.023	1.99	+0.94	0.15	2.25	8.79
0402.3381+51.1632	Gaia EDR3 446079578071772416	02 49.21.164	+51 24.47.553	-1.798	+1.457	-0.298	13.7262	0.0030	0.2629	2333	86	+0.042	0.012	1.83	+0.88	0.09	2.27	8.71
0406.2665+57.4649	Gaia EDR3 446079578071772416	02 49.03.984	+57 23.53.658	-1.765	+1.473	-0.035	13.9203	0.0031	0.259667	2299	86	+0.076	0.047	2.06	+0.03	0.08	2.87	8.50
0406.9585+53.9453	Gaia EDR3 446079578071772416	02 49.03.984	+53 15.03.984	-1.621	+1.255	-0.134	12.7750	0.0029	1.610395	2054	103	+0.161	0.032	1.55	+0.35	0.11	2.66	8.74
0407.5021+51.3159	Gaia EDR3 446079578071772416	02 49.03.984	+53 15.03.984	-1.621	+1.255	-0.134	12.7750	0.0029	1.610395	2054	103	+0.161	0.032	1.55	+0.35	0.11	2.66	8.74
0408.9303+44.3792	Gaia EDR3 44747445889969974	02 44.23.071	+44.45.24.540	-3.261	+1.917	-0.700	14.1646	0.0095	2.288997	3847	362	+0.46	0.046	1.19	+0.20	0.26	2.41	8.41
0409.7468+55.5067	Gaia EDR3 446079578071772416	02 49.10.030	+44.45.24.540	-3.261	+1.917	-0.700	14.1646	0.0095	2.288997	3847	362	+0.46	0.046	1.19	+0.20	0.26	2.41	8.41
0409.7474+55.5067	Gaia EDR3 44747445889969974	02 44.23.071	+44.45.24.540	-3.261	+1.917	-0.700	14.1646	0.0095	2.288997	3847	362	+0.46	0.046	1.19	+0.20	0.26	2.41	8.41
0409.7474+55.5067	Gaia EDR3 44747445889969974	02 44.23.071	+44.45.24.540	-3.261	+1.917	-0.700	14.1646	0.0095	2.288997	3847	362	+0.46	0.046	1.19	+0.20	0.26	2.41	8.41
0409.7474+55.5067	Gaia EDR3 44747445889969974	02 44.23.071	+44.45.24.540	-3.261	+1.917	-0.700	14.1646	0.0095	2.288997	3847	362	+0.46	0.046	1.19	+0.20	0.26	2.41	8.41
0409.7474+55.5067	Gaia EDR3 44747445889969974	02 44.23.071	+44.45.24.540	-3.261	+1.917	-0.700	14.1646	0.0095	2.288997	3847	362	+0.46	0.046	1.19	+0.20	0.26	2.41	8.41
0409.7474+55.5067	Gaia EDR3 44747445889969974	02 44.23.071	+44.45.24.540	-3.261	+1.917	-0.700	14.1646	0.0095	2.288997	3847	362	+0.46	0.046	1.19	+0.20	0.26	2.41	8.41
0409.7474+55.5067	Gaia EDR3 44747445889969974	02 44.23.071	+44.45.24.540	-3.261	+1.917	-0.700	14.1646	0.0095	2.288997	3847	362	+0.46	0.046	1.19	+0.20	0.26	2.41	8.41
0409.7474+55.5067	Gaia EDR3 44747445889969974	02 44.23.071	+44.45.24.540	-3.261	+1.917	-0.700	14.1646	0.0095	2.288997	3847	362	+0.46	0.046	1.19	+0.20	0.26	2.41	8.41
0409.7474+55.5067	Gaia EDR3 44747445889969974	02 44.23.071	+44.45.24.540	-3.261	+1.917	-0.700	14.1646	0.0095	2.288997	3847	362	+0.46	0.046	1.19	+0.20	0.26	2.41	8.41
0409.7474+55.5067	Gaia EDR3 44747445889969974	02 44.23.071	+44.45.24.540	-3.261	+1.917	-0.700	14.1646	0.0095	2.288997	3847	362	+0.46	0.046	1.19	+0.20	0.26	2.41	8.41
0409.7474+55.5067	Gaia EDR3 44747445889969974	02 44.23.071	+44.45.24.540	-3.261	+1.917	-0.700	14.1646	0.0095	2.288997	3847	362	+0.46	0.046	1.19	+0.20	0.26	2.41	8.41
0409.7474+55.5067	Gaia EDR3 44747445889969974	02 44.23.071	+44.45.24.540	-3.261	+1.917	-0.700	14.1646	0.0095	2.288997	3847	362	+0.46	0.046	1.19	+0.20	0.26	2.41	8.41
0409.7474+55.5067	Gaia EDR3 44747445889969974	02 44.23.071	+44.45.24.540	-3.261	+1.917	-0.700	14.1646	0.0095	2.288997	3847	362	+0.46	0.046	1.19	+0.20	0.26	2.41	8.41
0409.7474+55.5067	Gaia EDR3 44747445889969974	02 44.23.071	+44.45.24.540	-3.261	+1.917	-0.700	14.1646	0.0095	2.288997	3847	362	+0.46	0.046	1.19	+0.20	0.26	2.41	8.41
0409.7474+55.5067	Gaia EDR3 44747445889969974	02 44.23.071	+44.45.24.540	-3.261	+1.917	-0.700	14.1646	0.0095	2.288997	3847	362	+0.46	0.046	1.19	+0.20	0.26	2.41	8.41
0409.7474+55.5067	Gaia EDR3 44747445889969974	02 44.23.071	+44.45.24.540	-3.261	+1.917	-0.700	14.1646	0.0095	2.288997	3847	362	+0.46	0.046	1.19	+0.20	0.26	2.41	8.41
0409.7474+55.5067	Gaia EDR3 44747445889969974	02 44.23.071	+44.45.24.540	-3.261	+1.917	-0.700	14.1646	0.0095	2.288997	3847	362	+0.46	0.046	1.19	+0.20	0.26	2.41	8.41
0409.7474+55.5067	Gaia EDR3 44747445889969974	02 44.23.071	+44.45.24.540	-3.261	+1.917	-0.700	14.1646	0.0095	2.288997	3847	362	+0.46	0.046	1.19	+0.20	0.26	2.41	8.41
0409.7474+55.5067	Gaia EDR3 44747445889969974	02 44.23.071	+44.45.24.540	-3.261	+1.917	-0.700	14.1646	0.0095	2.288997	3847	362	+0.46	0.046	1.19	+0.20	0.26	2.41	8.41
0409.7474+55.5067	Gaia EDR3 44747445889969974	02 44.23.071	+44.45.24.540	-3.261	+1.917	-0.700	14.1646	0.0095	2.288997	3847	362	+0.46	0.046	1.19	+0.20	0.26	2.41	8.41
0409.7474+55.5067	Gaia EDR3 44747445889969974	02 44.23.071	+44.45.24.540	-3.261	+1.917	-0.700	14.1646	0.0095	2.288997	3847	362	+0.46	0.046	1.19	+0.20	0.26	2.41	8.41
0409.7474+55.5067	Gaia EDR3 44747445889969974	02 44.23.071	+44.45.24.540	-3.261	+1.917	-0.700	14.1646	0.0095	2.288997	3847	362	+0.46	0.046	1.19	+0.20	0.26	2.41	8.41
0409.7474+55.5067	Gaia EDR3 44747445889969974	02 44.23.071	+44.45.24.540	-3.261	+1.917	-0.700	14.1646	0.0095	2.288997	3847	362	+0.46	0.046	1.19	+0.20	0.26	2.41	8.41
0409.7474+55.5067	Gaia EDR3 44747445889969974	02 44.23.071	+44.45.24.540	-3.261	+1.917	-0.700	14.1646	0.0095	2.288997	3847	362	+0.46	0.046	1.19	+0.20	0.26	2.41	8.41
0409.7474+55.5067	Gaia EDR3 44747445889969974	02 44.23.071	+44.45.24.540	-3.261	+1.917	-0.700	14.1646	0.0095	2.288997	3847	362	+0.46	0.046	1.19	+0.20	0.26	2.41	8.41
0409.7474+55.5067	Gaia EDR3 44747445889969974	02 44.23.071	+44.45.24.540	-3.261	+1.917	-0.700	14.1646	0.0095	2.288997	3847	362	+0.46	0.046	1.19	+0.20	0.26	2.41	8.41
0409.7474+55.5067	Gaia EDR3 44747445889969974	02 44.23.071	+44.45.24.540	-3.261	+1.917	-0.700	14.1646	0										

**Table A1.** Essential data for our sample stars, sorted by increasing right ascension. The columns denote: (1) ATLAS object identifier. (2) Gaia EDR3 identifier. (3) Right ascension (J2000; Gaia EDR3). (4) Declination (J2000; Gaia EDR3). (5) X coordinate towards the Galactic centre. (6) Y coordinate in direction of Galactic rotation. (7) Z coordinate towards the north Galactic pole. (8) Magnitude in the  $G$  band (Gaia EDR3). (9)  $G$  mag error. (10) Rotational period (ATLAS). (11) Median of the photogeometric distance posterior,  $D$  (Gaia EDR3). (12) Distance error. (13) Dereddened colour index ( $BP - RP$ )<sub>0</sub> (Gaia EDR3). (14) Colour index error. (15) Absorption in the  $G$  band,  $A_G$ . (16) Intrinsic absolute magnitude in the  $G$  band,  $M_{G0}$ . (17) Absolute magnitude error. (18) Mass. (19) Logarithmic age.

(1)	(2)	(3)	(4)	(5)	(6)	(7)	(8)	(9)	(10)	(11)	(12)	(13)	(14)	(15)	(16)	(17)	(18)	(19)	
ID_ATO	ID_EDR3	RA(J2000) (hh mm ss.ss)	Dec(J2000) (dd mm ss.ss)	X (pc)	Y (pc)	Z (pc)	$G$ (mag)	$\epsilon_G$ (mag)	$P_{\text{rot}}$ (pc)	$D$ (pc)	$\epsilon_D$ (pc)	$\epsilon_{BP - RP}^0$ (mag)	$A_G$ (mag)	$\epsilon_{M_{G0}}$ (mag)	$M_{G0}$ (mag)	Mass (M <sub>sun</sub> )	log( $t$ ) (yr)		
1083.1990-35.5978	Gaia EDR3 18318189196465152	05:32:47.768	+35:35:52.246	-2.866	+0.356	+0.063	14.4956	0.0038	16.37762	2889	1978	+0.020	0.089	1.17	+1.00	0.13	2.27	8.64	
1084.68-36-35.5786	Gaia EDR3 1448105860160160248	05:38:44.070	+33:59:43.039	-2.204	+0.180	+0.046	13.8925	0.0033	16.83578	2185	977	+0.201	0.033	0.85	+1.33	0.10	2.00	8.89	
1084.93-21-37.2119	Gaia EDR3 18937713989842561664	05:37:15.93	+37:11.23.056	-2.177	+0.118	+0.032	14.6232	0.0057	18.38578	2046	116	+0.122	0.045	1.70	+1.33	0.12	2.05	8.78	
1086.1147-31.3873	Gaia EDR3 1448105860160160248	05:44:27.348	+31:15.13.117	-2.207	+0.165	+0.059	15.2939	0.0030	19.2094	2811	283	+0.252	0.013	0.08	+1.00	+0.23	1.22	1.77	8.78
1086.1972-24.3919	Gaia EDR3 33577117142074880	04:44:47.349	+24:23:31.095	-4.039	-0.267	-0.179	14.0418	0.0057	18.18867	4052	344	+0.029	0.087	1.50	-0.48	0.24	2.97	8.57	
1086.3092-11.25266	Gaia EDR3 33577017760238097064	04:45:20.142	+11.20.13.974	-1.615	-0.438	-0.271	12.0344	0.0030	21.2228	1695	56	+0.026	0.011	1.00	+1.33	0.08	1.95	9.00	
1086.5553-30.43940	Gaia EDR3 337612320316929	04:45:54.399	+23:20:21.113	-1.544	-0.130	-0.051	10.0361	0.0031	20.0390	1552	56	+0.026	0.015	1.43	+0.11	0.09	2.05	8.82	
1086.8555-29.9110	Gaia EDR3 1917943223016929	04:46:13.92	+20:20:42.949	-1.886	+0.327	+0.204	13.0681	0.0029	16.3391	1923	80	+0.123	0.007	0.62	+1.00	0.09	1.24	8.91	
1087.0495-24.3630	Gaia EDR3 3434303073674259856	05:47.25.566	+27.54.39.651	-3.241	-0.061	-0.011	15.0779	0.0042	19.4287	3242	552	+0.251	0.007	1.62	+0.37	0.24	2.14	8.91	
1087.1717-29.1833	Gaia EDR3 34568663575499950	05:48.16.096	+24:23:35.565	-1.727	+0.132	+0.100	14.4412	0.0029	16.3866	3242	552	+0.233	0.037	1.32	+1.88	0.10	1.83	8.79	
1087.2218-29.4548	Gaia EDR3 3445330353025848976	05:48.33.234	+29:17.34.565	-2.081	+0.093	+0.032	13.8925	0.0030	16.03880	2081	53	+0.228	0.017	0.99	+1.16	0.09	2.04	8.89	
1087.2751-25.3153	Gaia EDR3 345897093493465156	05:52.55.566	+38:39:10.186	-3.339	-0.370	-0.245	13.6732	0.0030	18.04969	3389	338	+0.028	0.013	1.36	+0.45	0.09	1.56	8.63	
1088.23-28.6228	Gaia EDR3 34570126132426156	05:52.56.13.92	+24:48.04.186	-1.886	+0.327	+0.204	15.4828	0.0032	19.3758	3190	284	+0.143	0.040	1.67	+1.13	0.13	2.05	8.82	
1089.0994-24.8012	Gaia EDR3 342905727549071776	05:56.13.92	+20:20:42.817	-1.886	+0.327	+0.204	15.4907	0.0032	19.3621	3670	456	+0.143	0.024	1.28	+1.13	0.13	2.08	8.87	
1089.7405-22.3852	Gaia EDR3 34448416682924892	05:58.33.253	+19:37.29.648	-2.279	-0.422	-0.099	14.4676	0.0030	18.0779	4235	4235	+0.177	0.060	1.60	+1.28	0.13	2.15	8.82	
1089.7405-22.3852	Gaia EDR3 3424448416682924892	05:58.33.253	+19:37.29.648	-2.279	-0.343	-0.026	14.4788	0.0031	18.0862	2751	169	+0.177	0.063	0.89	+1.00	0.09	1.21	8.73	
1089.7714-14.0001	Gaia EDR3 343381589015152548	05:59.07.71	+14:00.00.667	-3.347	-0.864	-0.295	14.0968	0.0044	19.14186	3469	171	+0.168	0.010	0.77	+0.56	0.14	2.82	8.19	
1090.0237-21.9017	Gaia EDR3 34323209171557504	06:00.15.078	+21.66.34.1	-2.155	-0.292	-0.039	14.6374	0.0030	18.5255	2174	112	+0.160	0.046	1.60	+1.33	0.11	2.02	8.84	
1090.3141-14.7489	Gaia EDR3 34545494936267776	06:15.15.306	+14:44.56.346	-3.380	-0.847	-0.248	14.8482	0.0031	19.3515	3493	370	+0.111	0.069	1.48	+0.61	0.26	2.31	8.80	
1090.55-31.0548	Gaia EDR3 34499126235100976	06:00.28.325	+17.03.17.267	-3.370	-0.065	-0.259	14.8417	0.0031	19.18545	3081	174	+0.127	0.016	1.36	+0.45	0.10	2.05	8.83	
1091.7794-32.5180	Gaia EDR3 342905727549071776	06:00.53.063	+20:20:42.817	-1.886	+0.327	+0.204	15.4602	0.0046	18.5265	1692	57	+0.035	0.010	0.62	+1.05	0.08	2.23	8.86	
1091.7794-32.5180	Gaia EDR3 3450617606393898886	06:00.53.063	+20:20:42.817	-1.886	+0.327	+0.204	15.4602	0.0046	18.5265	1692	57	+0.035	0.013	0.62	+1.05	0.15	1.94	8.86	
1091.7794-32.5180	Gaia EDR3 345061760639389886	06:00.53.063	+20:20:42.817	-1.886	+0.327	+0.204	15.4602	0.0046	18.5265	1692	57	+0.035	0.013	0.62	+1.05	0.15	1.94	8.86	
1091.7794-32.5180	Gaia EDR3 345061760639389886	06:00.53.063	+20:20:42.817	-1.886	+0.327	+0.204	15.4602	0.0046	18.5265	1692	57	+0.035	0.013	0.62	+1.05	0.15	1.94	8.86	
1091.7794-32.5180	Gaia EDR3 345061760639389886	06:00.53.063	+20:20:42.817	-1.886	+0.327	+0.204	15.4602	0.0046	18.5265	1692	57	+0.035	0.013	0.62	+1.05	0.15	1.94	8.86	
1091.7794-32.5180	Gaia EDR3 345061760639389886	06:00.53.063	+20:20:42.817	-1.886	+0.327	+0.204	15.4602	0.0046	18.5265	1692	57	+0.035	0.013	0.62	+1.05	0.15	1.94	8.86	
1091.7794-32.5180	Gaia EDR3 345061760639389886	06:00.53.063	+20:20:42.817	-1.886	+0.327	+0.204	15.4602	0.0046	18.5265	1692	57	+0.035	0.013	0.62	+1.05	0.15	1.94	8.86	
1091.7794-32.5180	Gaia EDR3 345061760639389886	06:00.53.063	+20:20:42.817	-1.886	+0.327	+0.204	15.4602	0.0046	18.5265	1692	57	+0.035	0.013	0.62	+1.05	0.15	1.94	8.86	
1091.7794-32.5180	Gaia EDR3 345061760639389886	06:00.53.063	+20:20:42.817	-1.886	+0.327	+0.204	15.4602	0.0046	18.5265	1692	57	+0.035	0.013	0.62	+1.05	0.15	1.94	8.86	
1091.7794-32.5180	Gaia EDR3 345061760639389886	06:00.53.063	+20:20:42.817	-1.886	+0.327	+0.204	15.4602	0.0046	18.5265	1692	57	+0.035	0.013	0.62	+1.05	0.15	1.94	8.86	
1091.7794-32.5180	Gaia EDR3 345061760639389886	06:00.53.063	+20:20:42.817	-1.886	+0.327	+0.204	15.4602	0.0046	18.5265	1692	57	+0.035	0.013	0.62	+1.05	0.15	1.94	8.86	
1091.7794-32.5180	Gaia EDR3 345061760639389886	06:00.53.063	+20:20:42.817	-1.886	+0.327	+0.204	15.4602	0.0046	18.5265	1692	57	+0.035	0.013	0.62	+1.05	0.15	1.94	8.86	
1091.7794-32.5180	Gaia EDR3 345061760639389886	06:00.53.063	+20:20:42.817	-1.886	+0.327	+0.204	15.4602	0.0046	18.5265	1692	57	+0.035	0.013	0.62	+1.05	0.15	1.94	8.86	
1091.7794-32.5180	Gaia EDR3 345061760639389886	06:00.53.063	+20:20:42.817	-1.886	+0.327	+0.204	15.4602	0.0046	18.5265	1692	57	+0.035	0.013	0.62	+1.05	0.15	1.94	8.86	
1091.7794-32.5180	Gaia EDR3 345061760639389886	06:00.53.063	+20:20:42.817	-1.886	+0.327	+0.204	15.4602	0.0046	18.5265	1692	57	+0.035	0.013	0.62	+1.05	0.15	1.94	8.86	
1091.7794-32.5180	Gaia EDR3 345061760639389886	06:00.53.063	+20:20:42.817	-1.886	+0.327	+0.204	15.4602	0.0046	18.5265	1692	57	+0.035	0.013	0.62	+1.05	0.15	1.94	8.86	
1091.7794-32.5180	Gaia EDR3 345061760639389886	06:00.53.063	+20:20:42.817	-1.886	+0.327	+0.204	15.4602	0.0046	18.5265	1692	57	+0.035	0.013	0.62	+1.05	0.15	1.94	8.86	
1091.7794-32.5180	Gaia EDR3 345061760639389886	06:00.53.063	+20:20:42.817	-1.886	+0.327	+0.204	15.4602	0.0046	18.5265	1692	57	+0.035	0.013	0.62	+1.05	0.15	1.94	8.86	
1091.7794-32.5180	Gaia EDR3 345061760639389886	06:00.53.063	+20:20:42.817	-1.886	+0.327	+0.204	15.4602	0.0046	18.5265	1692	57	+0.035	0.013	0.62	+1.05	0.15	1.94	8.86	
1091.7794-32.5180	Gaia EDR3 345061760639389886	06:00.53.063	+20:20:42.817	-1.886	+0.327	+0.204	15.4602	0.0046	18.5265	1692	57	+0.035	0.013	0.62	+1.05	0.15	1.94	8.86	
1091.7794-32.5180	Gaia EDR3 345061760639389886	06:00.53.063	+20:20:42.817	-1.886	+0.327	+0.204	15.4602	0.0046	18.5265	1692	57	+0.035	0.013	0.62	+1.05	0.15	1.94	8.86	
1091.7794-32.5180	Gaia EDR3 345061760639389886	06:00.53.063	+20:20:42.817	-1.886	+0.327	+0.204	15.4602	0.0046	18.5265	1692	57	+0.035	0.013	0.62	+1.05	0.15	1.94	8.86	
1091.7794-32.5180	Gaia EDR3 345061760639389886	06:00.53.063	+20:20:42.817	-1.886	+0.327	+0.204	15.4602	0.0046	18.5265	1692									

**Table A1.** Essential data for our sample stars, sorted by increasing right ascension. The columns denote: (1) ATLAS object identifier. (2) Gaia EDR3 identifier. (3) Right ascension (J2000; Gaia EDR3). (4) Declination (J2000; Gaia EDR3). (5) X coordinate towards the Galactic centre. (6) Y coordinate in direction of Galactic rotation. (7) Z coordinate towards the north Galactic pole. (8) Magnitude in the *G* band (Gaia EDR3). (9) *G* mag error. (10) Rotational period (ATLAS). (11) Median of the photogeometric distance posterior, *D* (Gaia EDR3). (12) Distance error. (13) Dereddened colour index (*BP* – *RP*)<sub>0</sub> (Gaia EDR3). (14) Colour index error. (15) Absorption in the *G* band, *A<sub>G</sub>*. (16) Intrinsic absolute magnitude in the *G* band, *M<sub>G0</sub>*. (17) Absolute magnitude error. (18) Mass. (19) Logarithmic age.

(1)	(2)	(3)	(4)	(5)	(6)	(7)	(8)	(9)	(10)	(11)	(12)	(13)	(14)	(15)	(16)	(17)	(18)	(19)	
ID_ATO	ID_EDR3	RA(J2000)	Dec(J2000)	X (kpc)	Y (kpc)	Z (kpc)	<i>G</i> (mag)	<i>e</i> <sub>–G</sub> (mag)	<i>P<sub>rot</sub></i> (pe)	<i>D</i> (pc)	<i>e</i> <sub>–D</sub> (pc)	( <i>BP</i> – <i>RP</i> ) <sub>0</sub> (mag)	<i>e</i> <sub>(<i>BP</i> – <i>RP</i>)<sub>0</sub> (mag)</sub>	<i>M<sub>G0</sub></i> (mag)	<i>e</i> <sub><i>M<sub>G0</sub></i></sub> (mag)	Mass (M <sub>sun</sub> )	log <sub>10</sub> (yrs)		
J103.3079+10.5510	Gaia EDRS 3.159021155714729872	06:53:13.988	+10:33:03.668	-26.13	-1.148	+0:259	13.5394	0.0035	1.542512	2865	181	+0:029	0.044	0.20	+1.06	0.14	2.23	8.65	
J103.8302+21.8643	Gaia EDRS 3.293586380127392	06:55:19.774	+21.51:18.860	-1.340	-1.141	-0:0344	13.7489	0.0031	1.585837	3846	284	+0:030	0.28	0.33	+2.63	0.09	1.55	8.89	
J103.8576+00.4954	Gaia EDRS 3.1124972453310952936	06:55:25.828	+00:24:45.490	-3.195	-2.557	-0:0324	13.9587	0.0034	1.598371	3134	309	+0:027	0.283	0.69	+1.71	0.11	1.94	8.53	
J104.5104+01.8853	Gaia EDRS 3.1112053528466024960	06:58:22.966	+01:50:07.370	-3.195	-2.557	-0:0324	13.7489	0.0031	1.585837	3846	284	+0:030	0.28	0.33	+2.63	0.09	1.55	8.89	
J105.0327+06.1169	Gaia EDRS 3.129891734276889044	07:00:07.0102	+06:07:01.002	-3.113	-1.688	-0:0292	13.9587	0.0034	1.598371	3553	326	+0:124	0.019	0.62	+0.56	0.14	2.32	8.80	
J105.3860+21.3214	Gaia EDRS 3.10960261734276889044	07:01:32.062	+21:17:20.700	-0.803	-1.071	-0:174	13.6448	0.0028	1.800013	1350	236	+0:337	0.009	0.41	+2.58	0.04	1.50	9.24	
J105.5347+07.9977	Gaia EDRS 3.10960261734276889044	07:02:08.333	+01:54:27.955	-2.662	-1.923	-0:087	13.8002	0.0036	2.944283	3285	149	+0.964	0.048	0.64	+0.57	0.14	1.0	8.60	
J105.6394+13.1320	Gaia EDRS 3.104481134388768870375744	07:03:34.191	+13:07:55.388	-1.729	-1.234	-0:1546	13.5845	0.0029	1.537205	3808	410	+0:118	0.044	0.44	+0.27	0.24	2.07	8.87	
J105.9212+15.5797	Gaia EDRS 3.1048906440192	07:04:34.191	+16:46:09.409	-0.988	-1.02	-0:012	12.5845	0.0030	1.616409	3192	419	+0.912	0.011	0.51	+1.44	0.13	1.97	8.87	
J105.9294+02.6372	Gaia EDRS 3.11563665304679444176	07:03:34.056	+02:38.255	-2.351	-1.468	-0:190	14.1671	0.0031	2.226779	2778	204	+0:066	0.027	0.39	+1.54	0.16	2.04	8.52	
J106.2127+00.9740	Gaia EDRS 3.107894839436434434	07:04:51.051	+01:47:32.322	-1.803	-2.233	-0:093	14.3678	0.0034	2.670824	3634	213	+0:013	0.047	0.38	+0.97	0.19	2.28	8.63	
J106.4471+03.7806	Gaia EDRS 3.1044877748373091784	07:05:47.370	+03:46:05.281	-2.865	-1.983	-0:139	14.9067	0.0037	3.2774142	2566	334	+0:280	0.111	1.10	+1.69	0.37	1.85	8.95	
J106.5589+18.8987	Gaia EDRS 3.1044457760205744	07:06:52.687	+18:33:03.969	-1.738	-1.882	-0:137	14.8783	0.0032	1.2584	2750	142	+0:29	0.16	0.40	+0.30	0.11	2.16	8.92	
J106.7274+15.1516	Gaia EDRS 3.1044877748373091784	07:07:08.333	+15:06:59.194	-1.738	-1.266	-0:163	12.46:02.633	-1.909	-0.986	-1.02	-1.02	+0.157	0.006	0.43	+1.37	0.05	2.01	8.83	
J107.2480+12.7673	Gaia EDRS 3.10326122442630400	07:12:26.923	+12:45:20.208	-1.908	-1.518	-0:242	12.5842	-1.354	-1.274	-0:019	13.1451	0.0030	1.944000	1858	46	+0.157	0.006	0.43	8.87
J108.1121+08.8579	Gaia EDRS 3.10483122442630400	07:12:26.923	+12:45:20.208	-1.908	-1.518	-0:242	12.5842	-1.354	-1.274	-0:019	14.0242	0.0030	1.944000	3012	88	+0.156	0.013	1.51	8.63
J108.1707+08.2617	Gaia EDRS 3.10517566777483653376	07:12:26.922	+08:15:42.222	-2.233	-2.051	-0:048	12.5842	-1.354	-1.274	-0:019	13.9230	0.0031	1.732936	3012	87	+0.156	0.013	1.51	8.72
J108.273-11.0753	Gaia EDRS 3.104555353553488768	07:13:05.355	+11:04:31.191	-2.121	-2.139	-0:016	15.4240	0.0037	1.732936	3012	87	+0.156	0.013	1.51	+0.27	0.18	2.50	8.72	
J108.3588+12.4968	Gaia EDRS 3.1043553535175008	07:13:05.355	+12:26:48.781	-1.965	-2.074	-0:044	14.4735	0.0029	1.978432	2857	122	+0.116	0.014	0.85	+1.34	0.09	2.05	8.77	
J108.6705+07.3062	Gaia EDRS 3.1034662190664045652	07:14:43.883	+07:18:23.381	-2.096	-1.893	-0:089	14.9067	0.0032	1.607134	3090	96	+0.087	0.014	0.56	+0.31	0.11	2.03	8.64	
J108.705-20.4362	Gaia EDRS 3.10500017880632576	07:14:49.264	+20:26:04.16	-1.062	-1.434	-0:133	13.2960	0.0028	2.258920	2784	18	+0.216	0.026	0.55	+1.51	0.05	1.95	8.89	
J108.7797+22.5861	Gaia EDRS 3.102782779847352454	07:15:17.43.5	+22.58.074	-2.35	-2.316	-0:075	14.2677	0.0032	1.466651	3787	119	+0.084	0.024	0.63	+0.18	0.12	2.12	8.77	
J109.4314+15.7080	Gaia EDRS 3.1031753303676416	07:15:42.350	+15:42:28.802	-2.245	-2.687	-0:089	14.9541	0.0032	1.536764	3516	344	+0.250	0.141	0.42	+0.82	0.21	2.18	8.87	
J109.5054+15.0571	Gaia EDRS 3.103263754683653376	07:15:49.315	+15:49:31.86	-1.902	-1.507	-0:031	12.6786	0.0029	1.616409	3268	322	+0.036	0.011	0.50	+0.27	0.12	2.10	8.62	
J109.7734+07.1470	Gaia EDRS 3.103786223288	07:19:45.632	+07:08:49.261	-2.478	-2.267	-0:167	13.9320	0.0031	2.2265	2786	183	+0.039	0.050	0.44	+0.84	0.17	2.44	8.50	
J110.170723+23.4818	Gaia EDRS 3.106156066025792	07:20:41.570	+12.28:54.704	-1.227	-1.895	-0:176	14.9461	0.0029	1.678078	2656	15	+0.056	0.016	0.71	+0.27	0.18	2.50	8.72	
J110.3588+12.4968	Gaia EDRS 3.1043553535175008	07:21:36.123	+12:26:48.781	-1.965	-2.074	-0:044	14.4735	0.0029	1.978432	2857	122	+0.116	0.014	0.85	+1.34	0.09	2.05	8.77	
J110.667-07.3062	Gaia EDRS 3.104662190664045652	07:21:00.190	+07:18:31.381	-1.838	-1.664	-0:285	14.9067	0.0032	1.607134	3090	96	+0.087	0.014	0.56	+0.31	0.11	2.03	8.64	
J110.7507+12.0207	Gaia EDRS 3.10500017880632576	07:21:00.190	+12:01:14.838	-1.563	-1.278	-0:180	14.9108	0.0036	1.607134	3090	96	+0.087	0.014	0.56	+0.31	0.11	2.03	8.64	
J110.7625+03.2520	Gaia EDRS 3.105980010753303676416	07:21:00.190	+03:15:07.028	-1.747	-2.518	-0:122	14.9108	0.0036	1.607134	3090	96	+0.087	0.014	0.56	+0.31	0.11	2.03	8.64	
J110.3902+17.5039	Gaia EDRS 3.102782779847352454	07:21:31.33.5	+17.51.50.7	-2.174	-2.385	-0:075	14.2688	0.0032	1.570797	4023	305	+0.051	0.029	0.65	+0.27	0.12	2.25	8.67	
J111.2165+23.1396	Gaia EDRS 3.106199369669162935632	07:23:08.2642	+23.13.26.642	-1.732	-2.936	-0:112	14.6048	0.0033	1.424933	3411	251	+0.054	0.043	0.43	+0.88	0.16	2.25	8.68	
J111.2196+06.1412	Gaia EDRS 3.106199369669162935632	07:23:08.2642	+06:14:26.481	-1.732	-2.936	-0:112	14.6048	0.0033	1.424933	3411	251	+0.054	0.043	0.43	+0.88	0.16	2.25	8.68	
J111.2676+19.4971	Gaia EDRS 3.104767630308750088	07:24:28.792	+19:49:26.898	-1.429	-1.929	-0:027	13.5621	0.0031	1.769139	2468	70	+0.072	0.078	0.75	+0.27	0.12	2.25	8.73	
J111.2843+20.5088	Gaia EDRS 3.10460315564992000	07:24:31.31.20	+20:49:26.898	-1.427	-1.929	-0:027	13.5621	0.0031	1.769139	2468	70	+0.072	0.078	0.75	+0.27	0.12	2.25	8.73	
J111.3387+19.1434	Gaia EDRS 3.101861031237970084	07:25:32.740	+19:40:24.906	-1.468	-2.086	-0:123	14.5551	0.0031	1.723555	551	74	+0.002	0.043	1.17	+0.09	0.06	2.16	8.81	
J111.5306+15.0738	Gaia EDRS 3.10208781000175364	07:34:47.364	+15:04:36.126	-1.865	-2.086	-0:123	14.5551	0.0031	1.723555	551	74	+0.002	0.043	1.17	+0.09	0.06	2.16	8.81	
J111.5307+18.5902	Gaia EDRS 3.10207845901247671472	07:40:32.301	+18:34:28.389	-1.268	-1.767	-0:029	14.6235	0.0032	1.616699	317	67	+0.033	0.029	0.63	+0.27	0.12	2.25	8.66	
J111.5521+25.5094	Gaia EDRS 3.10415416038972352268	07:40:45.202	+25:50:35.884	-1.490	-2.084	-0:078	14.3476	0.0032	1.542935	3411	251	+0.054	0.043	0.43	+0.88	0.16	2.25	8.68	
J111.5526+17.0845	Gaia EDRS 3.105173171308522000	07:45:35.354	+17:05:44.005	-1.701	-2.755	-0:163	14.2684	0.0032	1.542935	3420	303	+0.054	0.034	0.65	+0.27	0.12	2.25	8.66	
J111.5542+24.8845	Gaia EDRS 3.10642526099572920	07:46:34.93.20	+24:48:44.240	-1.858	-2.384	-0:070	15.1178	0.0030	1.682934	3774	275	+0.201	0.026	0.75	+0.27	0.12	2.25	8.66	
J111.6092+28.4220	Gaia EDRS 3.10484774743974440	07:37:31.36.576	+28:42:33.392	-1.557	-2.265	-0:001	13.8852	0.0032	1.590725	302	183	+0.089	0.10	1.14	+0.20	0.07	2.07	8.82	
J111.6243+14.2924	Gaia EDRS 3.1072290747750084	07:39:22.10.20	+14:20:40.140	-1.211	-1.929	-0:060	14.3642	0.0032	1.542935	3278	104	+0.156	0.029	0.75	+0.27	0.12	2.25	8.69	
J111.6258+10.1802	Gaia EDRS 3.10378001031237970084	0																	

**Table A1.** Essential data for our sample stars, sorted by increasing right ascension. The columns denote: (1) ATLAS object identifier. (2) Gaia EDR3 identifier. (3) Right ascension (J2000; Gaia EDR3). (4) Declination (J2000; Gaia EDR3). (5) X coordinate towards the Galactic centre. (6) Y coordinate in direction of Galactic rotation. (7) Z coordinate towards the north Galactic pole. (8) Magnitude in the  $G$  band (Gaia EDR3). (9)  $G$  mag error. (10) Rotational period (ATLAS). (11) Median of the photogeometric distance posterior,  $D$  (Gaia EDR3). (12) Distance error. (13) Dereddened colour index  $(BP - RP)_0$  (Gaia EDR3). (14) Colour index error. (15) Absorption in the  $G$  band,  $A_G$ . (16) Intrinsic absolute magnitude in the  $G$  band,  $M_{G0}$ . (17) Absolute magnitude error. (18) Mass. (19) Logarithmic age.

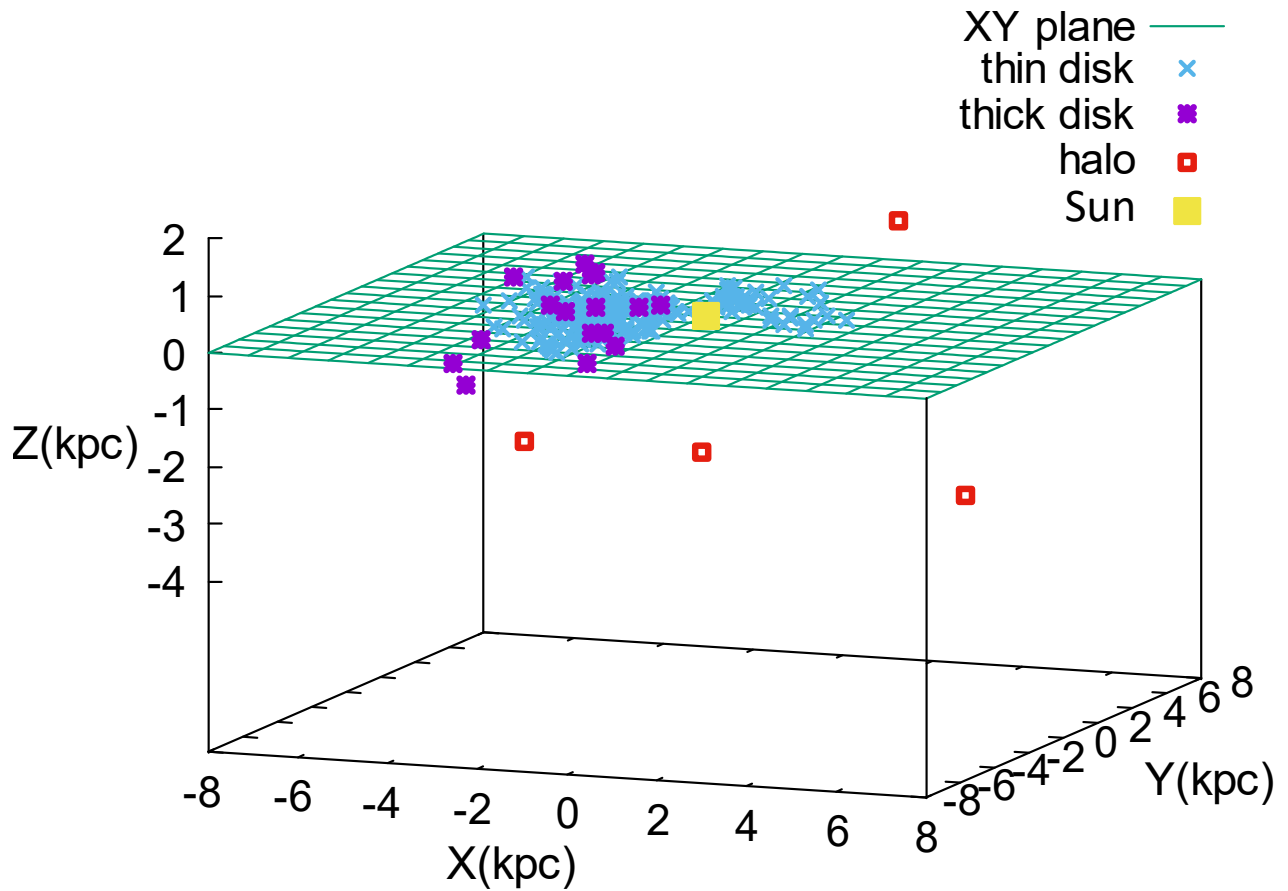


**Figure B1.** Distribution of our sample stars in the Galactic [XYZ] plane. Stars were assigned as probable members of the thin disk, the thick disk and the halo according to the scale heights provided by [Ojha \(2001\)](#) and [Aumer & Binney \(2017\)](#).

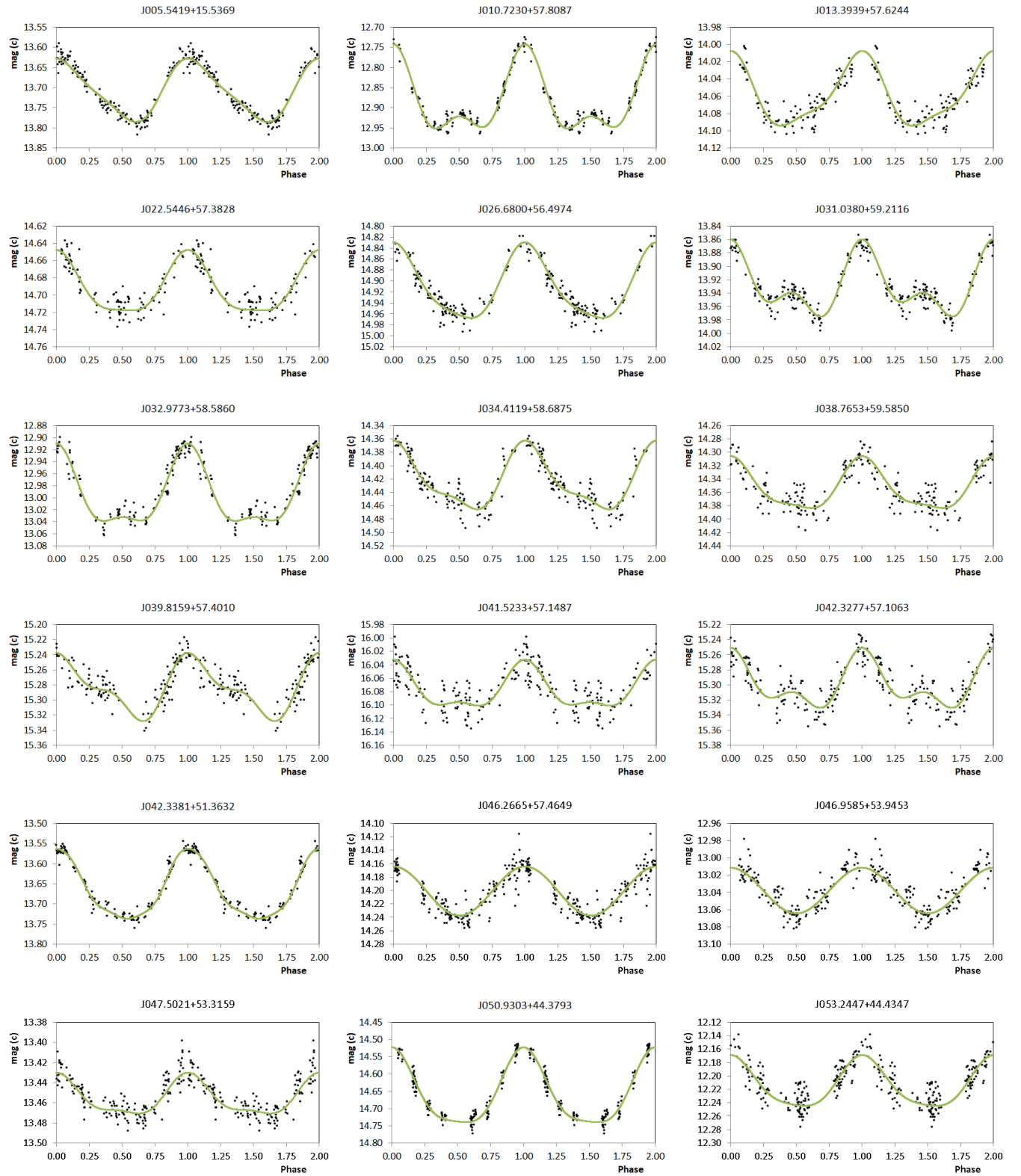


**Figure C1.** Sample page presenting the light curves of the first 16 objects in Table A1, folded with the periods listed therein. The full set of light curves is available online.